Available online at www.sciencedirect.com

SCIENCE DIRECT®

Coastal Engineering 51 (2004) 883–915

Coastal Engineering
An International Journal for Coastal, Harbour and Offshore Engineers

www.elsevier.com/locate/coastaleng

Development and validation of a three-dimensional morphological model

G.R. Lesser[a,*], J.A. Roelvink[a,b], J.A.T.M. van Kester[a], G.S. Stelling[b]

[a]WL/Delft Hydraulics, P.O. Box 177, 2600 MH Delft, The Netherlands
[b]Faculty of Civil Engineering and Geosciences, Hydraulic and Offshore Engineering Division, Delft University of Technology, Delft, The Netherlands

Available online 25 August 2004

Abstract

Computer modeling of sediment transport patterns is generally recognized as a valuable tool for understanding and predicting morphological developments. In practice, state-of-the-art computer models are one- or two-dimensional (depth-averaged) and have a limited ability to model many of the important three-dimensional flow phenomena found in nature. This paper presents the implementation and validation of sediment transport formulations within the proven DELFT3D three-dimensional (hydrostatic, free surface) flow solver. The paper briefly discusses the operation of the DELFT3D-FLOW module, presents the key features of the formulations used to model both suspended and bedload transport of noncohesive sediment, and describes the implemented morphological updating scheme. The modeling of the three-dimensional effects of waves is also discussed. Following the details of the implementation, the results of a number of validation studies are presented. The model is shown to perform well in several theoretical, laboratory, and real-life situations.

Keywords: Morphological; Model; DELFT3D; Validation; Hydrodynamic; Sediment transport; Coastal

1. Introduction

Morphodynamic models are indispensable tools that hydraulic engineers working in coastal, river, and estuarine systems use to analyze erosion problems, assess morphological impacts of human interference (at several scales), and to aid the design of coastal defenses. The last century has seen the development of these models from simple analytical models to 1D network, coastal profile, coastline, and multi-line models. In the 1980s and 1990s, depth-averaged two-dimensional (2DH) models were developed. Originating mainly in river engineering (e.g., Struiksma, 1985) the models often had sophisticated quasi-three-dimensional (quasi-3D) extensions to allow for spiral flow in bends. Later they were used in coastal areas where waves also play a crucial role in driving currents. For reviews of several such models, see de Vriend et al. (1993) and Nicholson et al. (1997). In the past, quasi-

* Corresponding author.
E-mail address: giles.lesser@wldelft.nl (G.R. Lesser).

0378-3839/$ - see front matter © 2004 Elsevier B.V. All rights reserved.
doi:10.1016/j.coastaleng.2004.07.014

3D concepts have also been implemented to account for cross-shore processes such as return flow, bed slope effects, and wave asymmetry effects (e.g., Watanabe et al., 1986; Bos et al., 1996). In coastal environments, such efforts were not entirely successful. The resulting transport fields were extremely sensitive to small disturbances resulting in very irregular patterns. Péchon and Teisson (1996) presented a morphological model based on a three-dimensional (3D) flow description, where the near-bed velocity was coupled with a local transport formula. This model also produced rather irregular results, which were at least partly due to the assumption of local equilibrium transport. More recently, Gessler et al. (1999) developed a 3D model for river morphology, which includes separate solvers for bedload transport and 3D suspended transport. It considers several size fractions of sediment and keeps track of the bed composition and evolution during each time step.

As a result, the present state-of-the-art is that quasi-3D and 3D approaches are successfully applied in river engineering, but their practical use in estuarine and coastal applications is limited. The use of straightforward 2DH morphological models has become more or less commonplace, especially in relatively large-scale applications in tidal inlets and estuaries. Ongoing increases in the computing power available to coastal engineers have meant that morphological simulations of years to decades have become feasible (e.g., Steijn et al., 1998; Roelvink et al., 2001).

However, in complex situations, several processes contribute to deviations of the velocity profile from a logarithmic one, such as curvature, acceleration and deceleration, wind- and wave-driven currents, density gradients, and Coriolis force. In addition, the shape of concentration profiles may differ substantially from those found under equilibrium conditions. Conditions such as these are common near the mouths of rivers, in complex estuarine geometries, and near structures. Predicting the behavior of such complex systems requires the use of numerical models or model systems that are able to simulate arbitrary combinations of processes within broad classes of problems.

The DELFT3D package, developed by WL|Delft Hydraulics in close cooperation with Delft University of Technology, is a model system that consists of a number of integrated modules which together allow the simulation of hydrodynamic flow (under the shallow water assumption), computation of the transport of water-borne constituents (e.g., salinity and heat), short wave generation and propagation, sediment transport and morphological changes, and the modeling of ecological processes and water quality parameters.

At the heart of the DELFT3D modeling framework is the FLOW module that performs the hydrodynamic computations and simultaneous (or "online") calculation of the transport of salinity and heat. This paper reports the recent addition of online computation of sediment transport and morphological changes within the DELFT3D-FLOW module. The main advantages of this online approach are the following: (1) three-dimensional hydrodynamic processes and the adaptation of nonequilibrium sediment concentration profiles are automatically accounted for in the suspended sediment calculations; (2) the density effects of sediment in suspension (which may cause density currents and/or turbulence damping) are automatically included in the hydrodynamic calculations; (3) changes in bathymetry can be immediately fed back to the hydrodynamic calculations; and (4) sediment transport and morphological simulations are simple to perform and do not require a large data file to communicate results between the hydrodynamic, sediment transport, and bottom updating modules.

The large number of processes included in DELFT3D-FLOW (wind shear, wave forces, tidal forces, density-driven flows and stratification due to salinity and/or temperature gradients, atmospheric pressure changes, drying and flooding of intertidal flats, etc.) mean that DELFT3D-FLOW can be applied to a wide range of river, estuarine, and coastal situations. The online sediment version allows calculation of morphological changes due to the transport, erosion, and deposition of both cohesive (mud) and noncohesive (sand) sediments in conjunction with any combination of the above processes. This makes the online sediment version of DELFT3D-FLOW especially useful for investigating sedimentation and erosion problems in complex hydrodynamic situations.

This paper begins by describing the physical formulations and numerical implementation used to model the transport of noncohesive (sand) sediment within DELFT3D-FLOW. It then presents several examples of validation studies that have been carried out using the online sediment version. The validation cases range from simple one- and two-dimensional theoretical tests to recreating three-dimensional physical model studies and prototype scale investigations. Unfortunately, space limitations prevent us from presenting the details of the implementation and example applications of the cohesive (mud) transport formulations in this paper. A thorough discussion of the modeling of cohesive sediments and sand–mud mixtures using DELFT3D-FLOW may be found in van Ledden (2001) and van Ledden and Wang (2001).

The validation cases presented here must be seen as the "tip of the iceberg" in terms of the full range of possible application areas of the model. However, to test the applicability of the new sediment transport model to typical coastal problems, we have selected the goal of simulating the morphological evolution of an initially straight beach behind an offshore breakwater. This is a typically complex coastal case that combines (1) wave-driven longshore and cross-shore currents, (2) flow acceleration, deceleration, and curvature, (3) nonequilibrium sediment concentrations due to waves and currents, (4) flooding and drying of computational cells, and (5) significant morphological changes.

The test cases leading to this "ultimate" test show the model's capability to represent these various aspects separately. We start with four simple test cases for which analytical solutions exist. These tests demonstrate the development of the expected equilibrium sediment concentration profile under stationary conditions and confirm the correct numerical implementation of the sediment pick-up, settling, and morphological development formulations. They also serve to indicate the required vertical grid resolution. Following this, three tests against laboratory flume experiments are presented. The effects of flow deceleration and acceleration are tested against a flume test of flow over a steep-sided trench conducted by van Rijn (1987). Flow curvature effects are tested against a curved flume experiment by Struiksma et al. (1984), and the combined effect of waves and currents on equilibrium sediment concentration profiles is tested against flume experiments conducted by Dekker and Jacobs (2000). The final test for which real-world validation data exists is a prototype-scale simulation of the morphological development that occurred around the extended breakwaters at the Dutch port of IJmuiden. This is the only tide-dominated simulation presented in this paper and is used to test (1) the morphological acceleration technique included in the model, (2) the difference between the results of 2DH and 3D models, (3) the effect of including a schematized wave climate in the morphological computation, and (4) the sensitivity of the model to selecting two alternative bed roughness formulations. Finally, we present the results of two simulations of theoretical situations previously discussed in the literature. In the first theoretical test, the new model is compared with an existing 2DH model for the case of a propagating Gaussian hump, which deforms into the well-known star shape discussed by de Vriend (1987). The test series is then concluded with the offshore breakwater case discussed by Nicholson et al. (1997).

The paper concludes with a discussion of the results so far and an overview of further development and testing that is foreseen in the near future.

2. Description of model formulations

2.1. Hydrodynamics

2.1.1. Governing equations

The DELFT3D-FLOW module solves the unsteady shallow-water equations in two (depth-averaged) or three dimensions. The system of equations consists of the horizontal momentum equations, the continuity equation, the transport equation, and a turbulence closure model. The vertical momentum equation is reduced to the hydrostatic pressure relation as vertical accelerations are assumed to be small compared to gravitational acceleration and are not taken into account. This makes the DELFT3D-FLOW model suitable for predicting the flow in shallow seas, coastal areas, estuaries, lagoons, rivers, and lakes. It aims to model flow phenomena of which the horizontal length and time scales are significantly larger than the vertical scales.

The user may choose whether to solve the hydrodynamic equations on a Cartesian rectangular, orthogonal curvilinear (boundary fitted), or spherical grid. In three-dimensional simulations, a boundary fitted (σ-coordinate) approach is used for the vertical grid direction. For the sake of clarity, the equations are presented in their Cartesian rectangular form only.

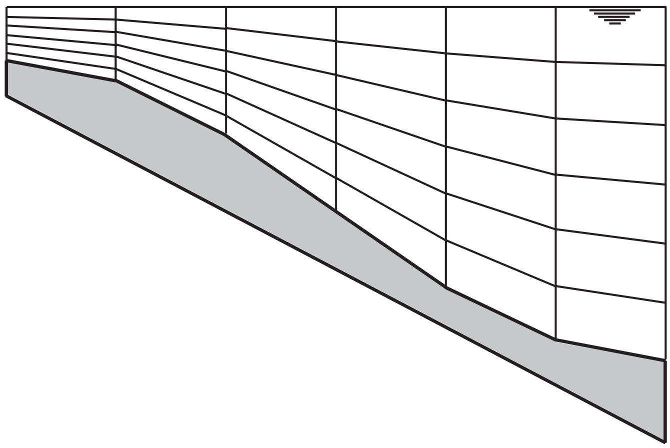

Fig. 1. An example of a vertical grid consisting of six equal thickness σ-layers.

2.1.1.1. Vertical σ-coordinate system. The vertical σ-coordinate is scaled as $(-1 \leq \sigma \leq 0)$

$$\sigma = \frac{z - \zeta}{h} \tag{1}$$

The flow domain of a 3D shallow water model consists of a number of layers. In a σ-coordinate system, the layer interfaces are chosen following planes of constant σ. Thus, the number of layers is constant over the horizontal computational area (Fig. 1). For each layer, a set of coupled conservation equations is solved. The partial derivatives in the original Cartesian coordinate system are expressed in σ-coordinates by use of the chain rule. This introduces additional terms (Stelling and van Kester, 1994).

2.1.1.2. Generalized Lagrangian Mean (GLM) reference frame. In simulations including waves, the hydrodynamic equations are written and solved in a GLM reference frame (Andrews and McIntyre, 1978; Groeneweg and Klopman, 1998; Groeneweg, 1999). In GLM formulation, the 2DH and 3D flow equations are very similar to the standard Eulerian equations; however, the wave-induced driving forces averaged over the wave period are more accurately expressed. The relationship between the GLM velocity and the Eulerian velocity is given by

$$U = u + u_{\mathrm{s}}$$

$$V = v + v_{\mathrm{s}} \tag{2}$$

where U and V are GLM velocity components, u and v are Eulerian velocity components, and u_{s} and v_{s} are the Stokes' drift components. For details and verification results, we refer to Walstra et al. (2000).

2.1.1.3. Hydrostatic pressure assumption. Under the so-called "shallow water assumption", the vertical momentum equation reduces to the hydrostatic pressure equation. Under this assumption, vertical acceleration due to buoyancy effects or sudden variations in the bottom topography is not taken into account. The resulting expression is

$$\frac{\partial P}{\partial \sigma} = -\rho g h \tag{3}$$

2.1.1.4. Horizontal momentum equations. The horizontal momentum equations are

$$\frac{\partial U}{\partial t} + U\frac{\partial U}{\partial x} + v\frac{\partial U}{\partial y} + \frac{\omega}{h}\frac{\partial U}{\partial \sigma} - fV = -\frac{1}{\rho_0}P_x + F_x + M_x + \frac{1}{h^2}\frac{\partial}{\partial \sigma}\left(\nu_{\mathrm{V}}\frac{\partial u}{\partial \sigma}\right)$$

$$\frac{\partial V}{\partial t} + U\frac{\partial V}{\partial x} + V\frac{\partial V}{\partial y} + \frac{\omega}{h}\frac{\partial V}{\partial \sigma} - fU = -\frac{1}{\rho_0}P_y + F_y + M_y + \frac{1}{h^2}\frac{\partial}{\partial \sigma}\left(\nu_{\mathrm{V}}\frac{\partial v}{\partial \sigma}\right) \tag{4}$$

in which the horizontal pressure terms, P_x and P_y, are given by (Boussinesq approximations)

$$\frac{1}{\rho_0}P_x = g\frac{\partial \zeta}{\partial x} + g\frac{h}{\rho_0}\int_{\sigma}^{0}\left(\frac{\partial \rho}{\partial x} + \frac{\partial \sigma'}{\partial x}\frac{\partial \rho}{\partial \sigma'}\right)d\sigma'$$

$$\frac{1}{\rho_0}P_y = g\frac{\partial \zeta}{\partial y} + g\frac{h}{\rho_0}\int_{\sigma}^{0}\left(\frac{\partial \rho}{\partial y} + \frac{\partial \sigma'}{\partial y}\frac{\partial \rho}{\partial \sigma'}\right)d\sigma' \quad (5)$$

The horizontal Reynold's stresses, F_x and F_y, are determined using the eddy viscosity concept (e.g., Rodi, 1984). For large-scale simulations (when shear stresses along closed boundaries may be neglected) the forces F_x and F_y reduce to the simplified formulations

$$F_x = \nu_H\left(\frac{\partial^2 U}{\partial x^2} + \frac{\partial^2 U}{\partial y^2}\right) \quad F_y = \nu_H\left(\frac{\partial^2 V}{\partial x^2} + \frac{\partial^2 V}{\partial y^2}\right) \quad (6)$$

in which the gradients are taken along σ-planes. In Eq. (4), M_x and M_y represent the contributions due to external sources or sinks of momentum (external forces by hydraulic structures, discharge or withdrawal of water, wave stresses, etc.).

2.1.1.5. Continuity equation. The depth-averaged continuity equation is given by

$$\frac{\partial \zeta}{\partial t} + \frac{\partial\left[h\bar{U}\right]}{\partial x} + \frac{\partial\left[h\bar{V}\right]}{\partial y} = S \quad (7)$$

in which S represents the contributions per unit area due to the discharge or withdrawal of water, evaporation, and precipitation.

2.1.1.6. Transport equation. The advection–diffusion equation reads

$$\frac{\partial[hc]}{\partial t} + \frac{\partial[hUc]}{\partial x} + \frac{\partial[hVc]}{\partial y} + \frac{\partial[\omega c]}{\partial \sigma} = h\left[\frac{\partial}{\partial x}\left(D_H\frac{\partial c}{\partial x}\right) + \frac{\partial}{\partial y}\left(D_H\frac{\partial c}{\partial y}\right)\right] + \frac{1}{h}\frac{\partial}{\partial \sigma}\left[D_V\frac{\partial c}{\partial \sigma}\right] + hS \quad (8)$$

in which S represents source and sink terms per unit area.

To solve these equations, the horizontal and vertical viscosity (ν_H and ν_V) and diffusivity (D_H and D_V) need to be prescribed. In DELFT3D-FLOW, the horizontal viscosity and diffusivity are assumed to be a superposition of three parts: (1) molecular viscosity, (2) "3D turbulence", and (3) "2D turbulence". The molecular viscosity of the fluid (water) is a constant value $O(10)^{-6}$. In a 3D simulation, "3D turbulence" is computed by the selected turbulence closure model (see the turbulence closure model section below). "2D turbulence" is a measure of the horizontal mixing that is not resolved by advection on the horizontal computational grid. 2D turbulence values may either be specified by the user as a constant or space-varying parameter, or can be computed using a subgrid model for horizontal large eddy simulation (HLES). The HLES model available in DELFT3D-FLOW is based on theoretical considerations presented by Uittenbogaard (1998) and is fully discussed by van Vossen (2000).

For use in the transport equation, the vertical eddy diffusivity is scaled from the vertical eddy viscosity according to

$$D_V = \frac{\nu V}{\sigma_c} \quad (9)$$

in which σ_c is the Prandtl–Schmidt number given by

$$\sigma_c = \sigma_{c0}F_{\sigma}(Ri) \quad (10)$$

where σ_{c0} is purely a function of the substance being transported. In the case of the algebraic turbulence model, F_{σ} (Ri) is a damping function that depends on the amount of density stratification present via the gradient Richardson's number (Simonin et al., 1989). The damping function, F_{σ} (Ri), is set equal to 1.0 if the $k-\varepsilon$ turbulence model is used, as the buoyancy term in the $k-\varepsilon$ model automatically accounts for turbulence-damping effects caused by vertical density gradients.

We note that the vertical eddy diffusivity used for calculating the transport of "sand" sediment constituents may, under some circumstances, vary somewhat from that given by Eq. (9) above. The diffusion coefficient used for sand sediment is described in more detail in Section 2.3.3.

2.1.1.7. Turbulence closure models. Several turbulence closure models are implemented in DELFT3D-FLOW. All models are based on the so-called "eddy viscosity" concept (Kolmogorov, 1942; Prandtl, 1945). The eddy viscosity in the models has the following form:

$$\nu_V = c_\mu{}' L\sqrt{k} \tag{11}$$

in which c'_μ is a constant determined by calibration, L is the mixing length, and k is the turbulent kinetic energy.

Two turbulence closure models are used in the simulations presented in this paper. The first is the "algebraic" turbulence closure model that uses algebraic/analytical formulas to determine k and L and therefore the vertical eddy viscosity. The second is the $k-\varepsilon$ turbulence closure model in which both the turbulent energy k and the dissipation ε are produced by production terms representing shear stresses at the bed, surface, and in the flow. The "concentrations" of k and ε in every grid cell are then calculated by transport equations. The mixing length L is determined from ε and k according to

$$L = c_D \frac{k\sqrt{k}}{\varepsilon} \tag{12}$$

in which c_D is another calibration constant.

2.1.2. Boundary conditions

To solve the systems of equations, the following boundary conditions are required.

2.1.2.1. Bed and free surface boundary conditions. In the σ-coordinate system, the bed and the free surface correspond with σ-planes. Therefore, the vertical velocities at these boundaries are simply

$$\omega(-1) = 0 \quad \text{and} \quad \omega(0) = 0 \tag{13}$$

Friction is applied at the bed as follows:

$$\frac{\nu_V}{h}\frac{\partial u}{\partial \sigma}\bigg|_{\sigma=-1} = \frac{\tau_{bx}}{\rho} \qquad \frac{\nu_V}{h}\frac{\partial v}{\partial \sigma}\bigg|_{\sigma=-1} = \frac{\tau_{by}}{\rho} \tag{14}$$

where τ_{bx} and τ_{by} are bed shear stress components that include the effects of wave–current interaction.

Friction due to wind stress at the water surface may be included in a similar manner although this is not used in the simulations presented in this paper. For the transport boundary conditions, the vertical diffusive fluxes through the free surface and bed are set to zero.

2.1.2.2. Lateral boundary conditions. Along closed boundaries, the velocity component perpendicular to the closed boundary is set to zero (a free-slip condition). At open boundaries, one of the following types of boundary conditions must be specified: water level, velocity (in the direction normal to the boundary), discharge, or linearised Riemann invariant (weakly reflective boundary condition; Verboom and Slob, 1984). Additionally, in the case of 3D models, the user must prescribe the use of either a uniform or logarithmic velocity profile at inflow boundaries.

For the transport boundary conditions, we assume that the horizontal transport of dissolved substances is dominated by advection. This means that at an open inflow boundary, a boundary condition is needed. During outflow, the concentration must be free. DELFT3D-FLOW allows the user to prescribe the concentration at every σ-layer using a time series. For sand sediment fractions, the local equilibrium sediment concentration profile may be used.

2.1.3. Solution procedure

DELFT3D-FLOW is a numerical model based on finite differences. To discretize the 3D shallow water equations in space, the model area is covered by a rectangular, curvilinear, or spherical grid. It is assumed that the grid is orthogonal and well structured. The variables are arranged in a pattern called the Arakawa C-grid (a staggered grid). In this arrangement, the water level points (pressure points) are defined in the center of a (continuity) cell; the velocity components are perpendicular to the grid cell faces where they are situated (see Fig. 2).

2.1.3.1. Hydrodynamics. For the simulations presented in this paper, an alternating direction implicit (ADI) method is used to solve the continuity and horizontal momentum equations (Leendertse, 1987). The advantage of the ADI method is that the implicitly integrated water levels and velocities are coupled along grid lines, leading to systems of equations with a small band width. Stelling (1984) extended the ADI method of

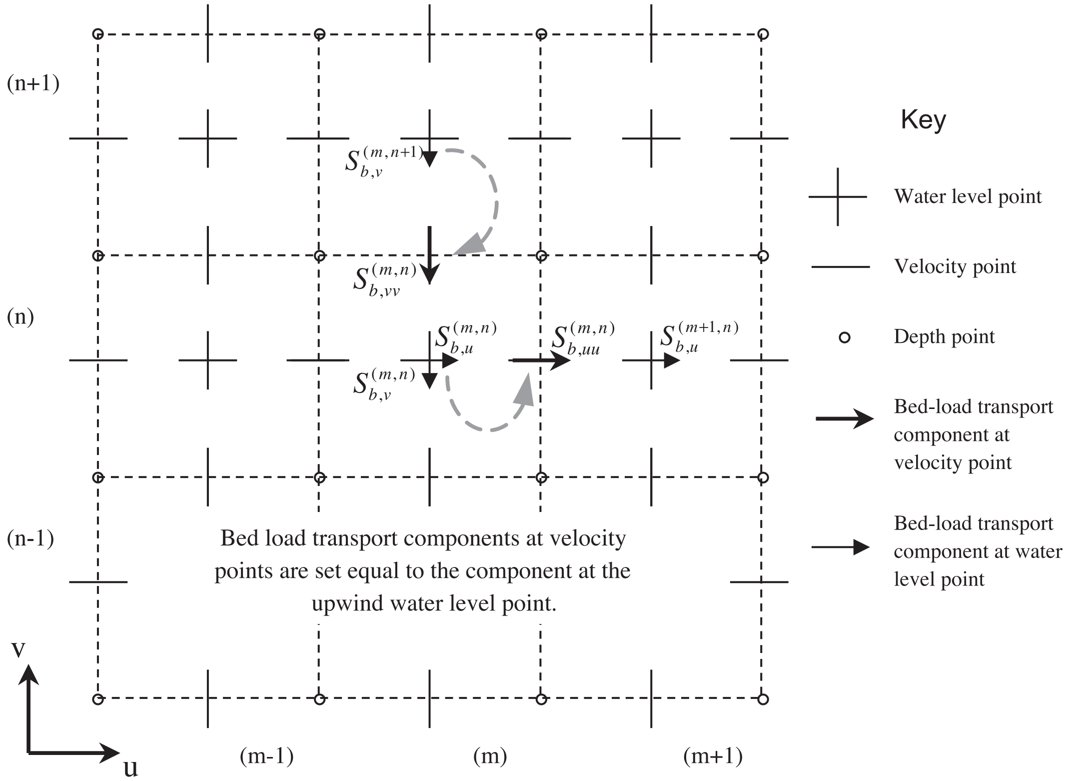

Fig. 2. The DELFT3D staggered grid showing the upwind method of setting bedload sediment transport components at velocity points. Water-level points are located in the center of the sediment control volumes.

Leendertse with a special approach for the horizontal advection terms. This approach splits the third-order upwind finite-difference scheme for the first derivative into two second-order consistent discretizations, a central discretization, and an upwind discretization, which are successively used in both stages of the ADI scheme. The scheme is denoted as a "cyclic method" (Stelling and Leendertse, 1991). This leads to a method that is computationally efficient, at least second-order accurate, and stable at Courant numbers of up to approximately 10. The diffusion tensor is redefined in the σ-coordinate system assuming that the horizontal length scale is much larger than the water depth (Mellor and Blumberg, 1985) and that the flow is of boundary-layer type.

The vertical velocity, ω, in the σ-coordinate system, is computed from the continuity equation

$$\frac{\partial \omega}{\partial \sigma} = -\frac{\partial \zeta}{\partial t} - \frac{\partial [hU]}{\partial x} - \frac{\partial [hV]}{\partial y} \tag{15}$$

by integrating in the vertical from the bed to a level σ. At the surface, the effects of precipitation and evaporation are taken into account. The vertical velocity, ω, is defined at the iso-σ-surfaces. ω is the vertical velocity relative to the moving σ-plane and may be interpreted as the velocity associated with up- or down-welling motions. The vertical velocities in the Cartesian coordinate system can be expressed in the horizontal velocities, water depths, water levels, and vertical coordinate velocities according to

$$w = \omega + U\left(\sigma\frac{\partial h}{\partial x} + \frac{\partial \zeta}{\partial x}\right) + V\left(\sigma\frac{\partial h}{\partial y} + \frac{\partial \zeta}{\partial y}\right) + \left(\sigma\frac{\partial h}{\partial t} + \frac{\partial \zeta}{\partial t}\right) \tag{16}$$

2.1.3.2. Transport. The transport equation is formulated in a conservative form (finite-volume approximation) and is solved using the so-called "cyclic method" (Stelling and Leendertse, 1991). For steep bottom slopes in combination with vertical stratification, horizontal diffusion along σ-planes introduces artificial vertical diffusion (Huang and Spaulding, 1996). DELFT3D-FLOW includes an algorithm to approximate the horizontal diffusion along z-planes in a σ-coordinate framework (Stelling and van Kester, 1994). In addition, a horizontal Forester filter (Forester, 1979) based on diffusion along σ-planes is applied to remove any negative concentration values that may occur. The Forester filter is mass conserving and does not cause significant amplitude losses in sharply peaked solutions.

2.2. Waves

2.2.1. General

Wave effects can also be included in a DELFT3D-FLOW simulation by running the separate DELFT3D-WAVE module. The DELFT3D-WAVE module must be accessed before running the FLOW module. This will result in a communication file being stored that contains the results of the wave simulation (RMS wave height, peak spectral period, wave direction, mass fluxes, etc.) on the same computational grid as is used by the FLOW module. The FLOW module can then read the wave results and include them in flow calculations. Wave simulations may be performed using the second-generation wave model HISWA (Holthuijsen et al., 1989) or the third-generation SWAN model (Holthuijsen et al., 1993). A significant practical advantage of using the SWAN model is that it can run on the same curvilinear grids as are commonly used for DELFT3D-FLOW calculations. Doing this reduces the effort required to prepare combined WAVE and FLOW simulations.

In situations where the water level, bathymetry, or flow velocity field change significantly during a FLOW simulation, it is often desirable to call the WAVE module more than once. The computed wave field can thereby be updated accounting for the changing water depths and flow velocities. This functionality is possible by way of the MORSYS steering module that can make alternating calls to the WAVE and FLOW modules. At each call to the WAVE module, the latest bed elevations, water elevations and, if desired, current velocities are transferred from FLOW.

2.2.2. Wave effects

In coastal seas, wave action may influence morphology for a number of reasons. The following processes are presently available in DELFT3D-FLOW.

(1) Wave forcing due to breaking (by radiation stress gradients) is modeled as a shear stress at the water surface (Svendsen, 1985; Stive and Wind, 1986). This radiation stress gradient is modeled using the simplified expression of Dingemans et al. (1987), where contributions other than those related to the dissipation of wave energy are neglected. This expression is as follows:

$$\vec{M} = \frac{D}{\omega}\vec{k} \tag{17}$$

in which $\vec{M}$=forcing due to radiation stress gradients (N/m^2), D=dissipation due to wave breaking (W/m^2), ω=angular wave frequency (rad/s), and $\vec{k}$=wave number vector (rad/m).

(2) The effect of the enhanced bed shear stress on the flow simulation is accounted for by following the parameterizations of Soulsby et al. (1993). Of the several models available, the simulations presented in this paper use the wave–current interaction model of Fredsoe (1984).

(3) The wave-induced mass flux is included and is adjusted for the vertically nonuniform Stokes drift (Walstra et al., 2000).

(4) The additional turbulence production due to dissipation in the bottom wave boundary layer and due to wave whitecapping and breaking at the surface is included as extra production terms in the k–ε turbulence closure model (Walstra et al., 2000).

(5) Streaming (a wave-induced current in the bottom boundary layer directed in the direction of wave propagation) is modeled as additional shear stress acting across the thickness of the bottom wave boundary layer (Walstra et al., 2000).

Processes 3, 4, and 5 have only recently been included in DELFT3D-FLOW and are essential if the (wave-averaged) effect of waves on the flow is to be correctly represented in 3D simulations. This is especially important for the accurate modeling of sediment transport in a nearshore coastal zone.

2.3. Suspended sediment transport

2.3.1. General

In the online sediment version of DELFT3D-FLOW, sediment is added to the list of constituents that can be computed by the transport solver described in Sections 2.1.1.6 and 2.1.3.2. Up to five sediment fractions may be defined. Each fraction must be classified as “mud” or “sand” as different formulations are used for the bed-exchange and settling velocity of these different types of sediment. In addition to the transport solver, several auxiliary formulations are required to fully describe the behavior of the sediment. The formulations implemented are described below.

2.3.1.1. Density effects. The equation of state used to calculate the density of the water with varying salinity and temperature (Eckart, 1958) is extended to include the density effect of sediment in suspension as follows:

$$\rho = \rho_{\mathrm{w}} + \sum_{l=1}^{\mathrm{LSED}} c_{\mathrm{vol}}^{(l)} \left(\rho_{\mathrm{s}}^{(l)} - \rho_{\mathrm{w}} \right) \tag{18}$$

in which ρ_{w} is the density of the water including salinity and temperature effects; $c_{\mathrm{vol}}^{(l)}$ is the volumetric concentration of sediment fraction l; $\rho_{\mathrm{s}}^{(l)}$ is the density of solid particles for sediment fraction l; LSED is the total number of sediment fractions.

2.3.1.2. Settling velocity. The settling velocity of sediment is modeled as a function of concentration and salinity, which may have a significant impact when modeling the transport of high concentrations of very fine cohesive sediments. However, for the sand transport cases considered in this paper, these effects are insignificant. The settling velocity of a sand sediment fraction is calculated following the method of van Rijn (1993) based on the nominal sediment diameter and the relative density of the sediment particles.

2.3.2. Sediment exchange with the bed

The exchange of sediment with the bed is implemented by way of sediment sources and sinks placed near the bottom of the flow. Separate pairs of sediment source and sink terms are required for each sediment fraction. These are calculated and located differently for mud sediment fractions than for sand sediment fractions.

For sand sediment fractions, we follow the approach of van Rijn (1993). A reference height is calculated based on the bed roughness. The sediment source and sink terms are located in the first computational cell that is entirely above the reference height (the reference cell). Cells that fall below the reference cell are assumed to rapidly respond to changes in the bed shear stress, and have a concentration equal to the concentration of the reference cell. The sediment concentration at the reference height is calculated using a formula adapted from van Rijn (1984) to include the presence of multiple sediment fractions

$$c_{\mathrm{a}} = f_{\mathrm{SUS}}\ \eta\ 0.015\ \rho_{\mathrm{s}} \frac{d_{50}}{a} \frac{T_{\mathrm{a}}^{1.5}}{D_{*}^{0.3}} \tag{19}$$

in which c_{a} is the mass concentration of the sediment at the reference height a; f_{SUS} is a user-specified calibration parameter (default value 1.0); η is the relative availability of the sediment fraction at the bed; T_{a} and D_{*} are the dimensionless bed shear stress and dimensionless particle diameter (as calculated by van Rijn, 1993), respectively. We note that T_{a} is computed from the flow velocity in the bottom computational layer by assumption of two logarithmic velocity profiles. First, a logarithmic velocity profile based on the apparent bed roughness (possibly enhanced by wave orbital motion) is assumed to exist between the mid-height of the bottom computational layer and the top of the wave boundary layer (if one exists). Then, a velocity profile based on the actual (specified) bed roughness is assumed to exist within the wave boundary layer. This allows the computation of u_{*}, and hence T_{a}, regardless of the relative heights of the middle of the bottom computational layer, the edge of the wave boundary layer, and the z_0 roughness height.

The sediment source and sink terms are then calculated assuming a linear concentration gradient between the calculated reference concentration at height a and the computed concentration in the reference cell. The terms are split so that the sediment source can be evaluated explicitly, whereas the sink must be included in the transport equation implicitly (Lesser, 2000). The resulting expressions are

$$\text{Source} = c_a\left(\frac{D_V}{\Delta z}\right)$$

$$\text{Sink} = c_{\text{kmx}}\left(\frac{D_V}{\Delta z} + w_s\right) \tag{20}$$

in which D_V is the vertical diffusion coefficient at the bottom of the reference cell, Δz is the vertical distance from the reference level a to the centre of reference cell, and c_{kmx} is the mass concentration of the sediment fraction in question in the reference cell (solved implicitly).

For mud sediment fractions, the source and sink terms are always located in the bottom computational cell and are computed with the well-known Partheniades and Krone formulations (Partheniades, 1965). For further details, refer to van Ledden (2001).

2.3.3. Vertical diffusion coefficient for sediment

For sand sediments, in situations without waves, σ_{c0} in Eq. (10) is set to 1.0 and van Rijn's β factor (used to describe the difference between fluid and granular diffusion; van Rijn, 1993) is included in Eq. (9). This results in

$$D_V = \beta\frac{\nu_V}{\sigma_c} \tag{21}$$

where

$$\beta = 1 + 2\left[\frac{w_s}{u_{*,c}}\right]^2$$

$$\text{limited to the range} \quad 1.0 \leq \beta \leq 1.5 \tag{22}$$

in which $u_{*,c}$ is the current-related bed shear velocity. Note that when the $k-\varepsilon$ turbulence closure model is selected, σ_c will also be equal to 1.0 in Eq. (21). For the algebraic turbulence model, σ_c is limited to the role of representing the turbulence damping effects of vertical density gradients. For this reason, van Rijn's ϕ factor (van Rijn, 1984) that also accounts for these effects is not implemented.

For simulations including waves, using the $k-\varepsilon$ turbulence closure model, the approach is similar to that described above, with one exception. As van Rijn's β factor is intended to apply to only the current-related mixing, the β factor applied to the total mixing computed by the $k-\varepsilon$ model is reduced according to the expression

$$\beta_{\text{eff}} = 1 + (\beta - 1)\frac{\tau_c}{\tau_w + \tau_c} \tag{23}$$

where τ_c is the bed shear stress due to current and τ_w is the bed shear stress due to waves. β_{eff} is then applied in place of β in Eq. (21).

For simulations including waves, using the algebraic turbulence model, a different approach is used for the vertical diffusion coefficient of sand sediment fractions. In this case, the diffusion coefficient is calculated using analytical expressions given by van Rijn (1993) for both the current- and wave-related turbulent mixing. The current-related mixing is calculated using the "parabolic constant" distribution recommended by van Rijn

$$\begin{aligned} z &< 0.5h \quad D_{V,c} = k\beta u_{*,c}z(1 - z/h) \\ z &\geq 0.5h \quad D_{V,c} = 0.25k\beta u_{*,c}h \end{aligned} \tag{24}$$

where $D_{V,c}$ is the vertical sediment diffusion coefficient due to currents, and $u_{*,c}$ is the current-related bed shear velocity. In the lower half of the water column, this expression produces similar turbulent mixing values to those produced by the standard algebraic turbulence closure model in current-only situations.

The wave-related mixing is calculated as

$$\begin{aligned} z \leq \delta_s \quad & D_{V,w} = D_{V,\text{bed}} = 0.004 D_* \delta_s \hat{U}_\delta \\ z \geq 0.5h \quad & D_{V,w} = D_{V,\text{max}} = 0.035 h H_s/T_p \\ \delta_s < z < 0.5h \quad & D_{V,w} = D_{V,\text{bed}} \\ & + \left[D_{V,\text{max}} - D_{V,\text{bed}}\right]\left[\frac{z - \delta_s}{0.5h - \delta_s}\right] \end{aligned} \tag{25}$$

where $D_{V,w}$ is the vertical sediment diffusion coefficient due to waves and δ_s is the thickness of the near-bed sediment mixing layer following van Rijn, and $\hat{U}_\delta$ is the peak wave orbital velocity at the edge of the wave boundary layer.

The total vertical sediment diffusion coefficient is then calculated as

$$D_V = \sqrt{D_{V,c}^2 + D_{V,w}^2} \tag{26}$$

where D_V is the vertical sediment diffusion coefficient used in the suspended sediment transport calculations for this sediment fraction.

For all sand sediment fractions, the vertical sediment diffusion coefficient for layers below the reference layer is set to a relatively high value. This ensures that the concentration of cells below the reference cell comes rapidly to equilibrium. The above calculation of the vertical sediment diffusion coefficient is repeated for each sediment fraction.

2.3.4. Suspended sediment correction vector

In the online-sediment version of DELFT3D-FLOW, the transport of suspended sediment is computed over the entire water column (from σ=−1 to σ=0). However, for sand sediment fractions, van Rijn regards sediment transported below the reference height, a, as belonging to "bedload" sediment transport that is computed separately as it responds almost instantaneously to changing flow conditions and feels the effects of bed slopes. To prevent double counting, the suspended sediment transport computed by the FLOW transport solver below the reference height a is estimated using simple central difference schemes for both advection, and diffusion and the result is stored as a "suspended sediment correction vector" ($S_{\mathrm{cor,uu}}$ and $S_{\mathrm{cor,vv}}$). The direction of the correction vector is reversed, and gradients in this vector are included in the computed morphological changes as described in Section 2.5.

2.4. Bedload sediment transport

Bedload transport is calculated for all sand sediment fractions following the approach described by van Rijn (1993). This accounts for the near-bed sediment transport occurring below the reference height a described above.

First, the magnitude and direction of the bedload sand transport are computed using one of two formulations presented by van Rijn depending on whether waves are present in the simulation. The computed sediment transport vectors are then relocated from water level points to velocity points using an "upwind" computational scheme to ensure numerical stability. Finally, the transport components are adjusted for bed-slope effects.

2.4.1. Basic formulation

2.4.1.1. Simulations without waves. For simulations without waves, the magnitude of the bedload transport on a horizontal bed is calculated using a formulation provided by van Rijn (personal communication, June 2000)

$$|S_b| = f_{\mathrm{BED}}\,\eta 0.5\rho_s d_{50} u_*{}' D_*^{-0.3} T \tag{27}$$

where $|S_b|$ is the bedload transport rate (kg/m/s); f_{BED} is a user-specified calibration factor (default value 1.0), which is included to allow users to adjust the overall significance of bedload sediment transport; η is the relative availability of the sediment fraction in the mixing layer; $u_*{}'$, D_*, and T are the effective bed shear velocity, the dimensionless particle diameter, and the dimensionless bed-shear stress (all following van Rijn), respectively. $u_*{}'$ and T are based on the computed velocity in the bottom computational layer.

In the absence of waves, the direction of the bedload transport is taken to be parallel with the flow in the bottom computational layer. Thus, the bedload vector components are given by

$$S_{\mathrm{b,u}} = \frac{u_{\mathrm{b,u}}}{|u_{\mathrm{b}}|}|S_{\mathrm{b}}|, \quad S_{\mathrm{b,v}} = \frac{u_{\mathrm{b,v}}}{|u_{\mathrm{b}}|}|S_{\mathrm{b}}| \tag{28}$$

where $u_{\mathrm{b,u}}$, $u_{\mathrm{b,v}}$, and $|u_{\mathrm{b}}|$ are the local bottom-layer flow velocity components and magnitude.

2.4.1.2. Simulations including waves. For simulations including waves, the magnitude and direction of the bedload transport on a horizontal bed are calculated using an approximation method developed by van Rijn (2001). This method includes an estimate of the effects of wave orbital velocity asymmetry on bedload sediment transport. The method computes the magnitude of the bedload transport as

$$|S_{\mathrm{b}}| = \eta 0.006\rho_{\mathrm{s}} w_{\mathrm{s}} M^{0.5} M_{\mathrm{e}}^{0.7} \tag{29}$$

where $|S_{\mathrm{b}}|$=magnitude of bedload transport (kg/m/s), η=relative availability of the sediment fraction in the mixing layer, M=sediment mobility number due to waves and currents, and M_e=excess sediment mobility number. M and M_e are computed as

$$M = \frac{v_{\mathrm{eff}}^2}{(s-1)gd_{50}} \tag{30}$$

$$M_e = \frac{(v_{\mathrm{eff}} - v_{\mathrm{cr}})^2}{(s-1)gd_{50}} \tag{31}$$

where

$$v_{\mathrm{eff}} = \sqrt{v_R^2 + U_{\mathrm{on}}^2} \tag{32}$$

in which s=relative sediment density (=ρ_s/ρ), v_{cr}=critical depth-averaged velocity for initiation of motion (based on a parameterization of the Shields curve), v_R=magnitude of an equivalent depth-averaged velocity computed from the (Eulerian) velocity in the bottom computational layer, assuming a logarithmic velocity profile, U_{on}=near-bed peak orbital velocity in onshore direction (in the direction on wave propagation) based on the significant wave height.

U_{on} (and U_{off} used below) are the high-frequency, near-bed orbital velocities due to short waves and are computed using a modification of the method of Isobe and Horikawa (1982). This method is a parameterization of fifth-order Stokes wave theory and third-order cnoidal wave theory. It can be used over a wide range of wave conditions and takes into account the nonlinear effects that occur as waves propagate in shallow water (Grasmeijer and van Rijn, 1998).

The direction of the bedload transport vector is determined by assuming that it is composed of two parts: (1) a part due to the current ($S_{b,c}$) that acts in the direction of the (Eulerian) near-bed current, and (2) a part due to the waves ($S_{b,w}$) that acts in the direction of wave propagation. The magnitudes of these two parts are determined as follows:

$$|S_{b,c}| = \frac{|S_b|}{\sqrt{1 + r^2 + 2|r|\cos\varphi}} \tag{33}$$

$$|S_{b,w}| = r|S_{b,c}| \tag{34}$$

where

$$r = \frac{(|U_{\mathrm{on}}| - v_{\mathrm{cr}})^3}{(|v_R| - v_{\mathrm{cr}})^3} \tag{35}$$

$S_{b,w}$=0 if r<0.01, $S_{b,c}$=0 if r>100, and φ=angle between current and wave directions.

Also included in the "bedload" transport vector is an estimation of the suspended sediment transport due to wave asymmetry effects. This is intended to model the effect of asymmetric wave orbital velocities on the transport of suspended material within approximately 0.5 m of the bed and accounts for the bulk of the suspended transport affected by high-frequency wave oscillations.

This wave-related suspended sediment transport is modeled using an approximation method proposed by van Rijn (2001):

$$|S_{s,w}| = \gamma U_A L_T \tag{36}$$

where $|S_{s,w}|$=magnitude of the wave-related suspended transport (kg/m/s), γ=phase lag coefficient (=0.2), U_A=velocity asymmetry value=$(U_{on}^4 - U_{off}^4)/(U_{on}^3 + U_{off}^3)$, and L_T=suspended sediment load=$0.007\rho_s d_{50} M$.

The three separate transport modes are then combined under the assumption that $S_{b,c}$ is in the direction of the (Eulerian) near-bed current and $S_{b,w}$ and $S_{s,w}$ are in the direction of wave propagation. This results in the following bedload transport components:

$$S_{b,u} = f_{\mathrm{BED}}\left[\frac{u_b}{|\vec{u}_b|}|S_{b,c}| + \left(f_{\mathrm{BEDW}}\, S_{b,w} + f_{\mathrm{SUSW}}\, S_{s,w}\right)\cos\phi\right]$$

$$S_{b,v} = f_{\mathrm{BED}}\left[\frac{u_b}{|\vec{u}_b|}|S_{b,c}| + \left(f_{\mathrm{BEDW}}\, S_{b,w} + f_{\mathrm{SUSW}}\, S_{s,w}\right)\sin\phi\right] \tag{37}$$

where f_{BED}=user-specified calibration factor (default value 1.0), f_{BEDW}=user-specified calibration factor (default value 1.0), f_{SUSW}=user-specified calibration factor (0.5 recommended for field cases, 1.0 for flumes), u_b, v_b, $\vec{u}_b$=Eulerian velocity components and vector in the bottom computational layer, and ϕ=local angle between the direction of wave propagation and the computational grid.

2.4.2. Upwind shift

The bedload transport vector components described above are computed at the water level points in the DELFT3D-FLOW staggered grid (e.g., $S_{b,u}$ in Fig. 2), as are the suspended-sediment sources and sinks. The bedload vector components at the velocity points (e.g., $S_{b,uu}$), around the perimeter of each cell control volume, are determined by transferring the appropriate vector components from the adjacent water level point half a grid cell "upwind", as indicated in Fig. 2. The upwind direction is based on the computed direction of the bedload transport vectors in the water level points. If the vector directions in adjacent water level points oppose, then a central scheme is used. This upwind shift ensures numerical stability and allows the implementation of an extremely simple morphological updating scheme, as described in Section 2.5 below.

In the example shown in Fig. 2, the bedload sediment transport components at the u- and v-velocity points of grid cell (m,n) are set as follows: in the u direction, the transport at the u-velocity point, $S_{b,uu}^{(m,n)}$, is set equal to the u-component of the transport computed at the upwind water level point, in this case, $S_{b,u}^{(m,n)}$. In the v direction, the transport at the v-velocity point, $S_{b,vv}^{(m,n)}$, is in this case set equal to $S_{b,v}^{(m,n+1)}$ because the bedload transport direction opposes the grid direction. Following the upwind shift, the bedload transports at the U and V velocity points are then modified for bed-slope effects.

2.4.3. Bed slope effects

As bedload transport is more-or-less continuously in contact with the bed, the slope of the bed affects the magnitude and direction of the bedload transport vector. A longitudinal slope in the direction of the bedload transport modifies the magnitude of the bedload vector as follows (modified from Bagnold, 1966):

$$S_{b,uu} = \alpha_s S_{b,uu}, \quad S_{b,vv} = \alpha_s S_{b,vv} \tag{38}$$

where

$$\alpha_s = 1 + f_{ALFABS} \times \left[\frac{\tan(\phi)}{\cos\left(\tan^{-1}\left(\frac{\partial z}{\partial s}\right)\right)\left(\tan(\phi) - \frac{\partial z}{\partial s}\right)} - 1 \right] \tag{39}$$

in which f_{ALFABS} is a user-specified tuning parameter, $\partial z/\partial s$ is the bed slope in the direction of the bedload transport (positive down), ϕ is the internal angle of friction of bed material (assumed to be 30°).

A transverse bed slope modifies the direction of the bedload transport vector. This modification is broadly based on the work of Ikeda (1982) and is computed as follows:

$$S_{b,uu} = S_{b,uu} - \alpha_n S_{b,vv}, \quad S_{b,vv} = S_{b,vv} + \alpha_n S_{b,uu} \tag{40}$$

where

$$\alpha_n = f_{ALFABN} \left(\frac{\tau_{b,cr}}{\tau_{b,cw}} \right)^{0.5} \frac{\partial z}{\partial n} \tag{41}$$

in which f_{ALFABN} is a user-specified coefficient (default 1.5), $\tau_{b,cr}$ is the critical bed shear stress, $\tau_{b,cw}$ is the bed shear stress due to current and waves, $\partial z/\partial n$ is the bed slope normal to the unadjusted bedload transport vector.

2.5. Morphodynamics

The quantity of each sediment fraction available at the bed is computed every half time step using simple bookkeeping for the control volume of each computational cell. This simple approach is made possible by the upwind shift of the bedload transport components described above, and is much less computationally intensive than the Lax–Wendroff bed updating scheme used in many other morphological models.

2.5.1. Suspended sediment transport

The net sediment change due to suspended sediment transport is calculated as follows:

$$\Delta s_{sus}^{(m,n)} = f_{MOR}(\text{Sink} - \text{Source})\Delta t \tag{42}$$

where f_{MOR} is the morphological acceleration factor (described in Section 2.5.2), Sink and Source are the suspended-sediment sink and source terms as given by Eq. (20) above, and Δt is the computational (half) time step.

The correction for suspended sediment transported below the reference height, a, is taken into account by including gradients in the suspended transport correction vector, S_{cor}, as follows:

$$\Delta s_{cor}^{(m,n)} = f_{MOR}\begin{pmatrix} S_{cor,uu}^{(m-1,n)}\Delta y^{(m-1,n)} - S_{cor,uu}^{(m,n)}\Delta y^{(m,n)} + \\ S_{cor,vv}^{(m,n-1)}\Delta x^{(m,n-1)} - S_{cor,vv}^{(m,n)}\Delta x^{(m,n)} \end{pmatrix} \times \frac{\Delta t}{A^{(m,n)}} \quad (43)$$

where $A^{(m,n)}$ is the area of the computational cell at location (m,n); $S_{cor,uu}^{(m,n)}$ and $S_{cor,vv}^{(m,n)}$ are the suspended-sediment correction vector components in the u and v directions, at the u and v velocity points of the computational cell at location (m,n); $\Delta x^{(m,n)}$ and $\Delta y^{(m,n)}$ are the widths of cell (m,n) in the x and y directions, respectively.

2.5.2. Bedload sediment transport

Similarly, the change in bottom sediment due to bedload transport is calculated as

$$\Delta s_{bed}^{(m,n)} = f_{MOR}\Big(S_{b,uu}^{(m-1,n)}\Delta y^{(m-1,n)} - S_{b,uu}^{(m,n)}\Delta y^{(m,n)} + S_{b,vv}^{(m,n-1)}\Delta x^{(m,n-1)} - S_{b,vv}^{(m,n)}\Delta x^{(m,n)}\Big)\frac{\Delta t}{A^{(m,n)}} \quad (44)$$

where $S_{b,uu}^{(m,n)}$ and $S_{b,vv}^{(m,n)}$ are the bedload sediment transport vector components at the u and v velocity points, respectively.

2.5.3. Total change in bed sediments

The total change in sediment is simply the sum of the change due to suspended load, the change due to the suspended-load correction vector, and the change due to bedload. This process is repeated for each sediment fraction.

2.5.4. Morphological acceleration factor

The morphological acceleration factor, f_{MOR}, is a device used to assist in dealing with the difference in time-scales between hydrodynamic and morphological developments. It works very simply by multiplying the changes in bed sediments by a constant factor, thereby effectively extending the morphological time step. Effectively

$$\Delta t_{morphology} = f_{MOR}\Delta t_{hydrodynamic} \quad (45)$$

This technique is very similar to the "elongated tide" technique proposed by Latteux (1995) and implies that long morphological simulations can be achieved using hydrodynamic simulations of only a fraction of the required duration. Obviously, there are limits to the morphological acceleration factor that can be applied, depending on the characteristics of the location under consideration. The selection of a suitable morphological acceleration factor remains a matter of judgement and sensitivity testing for the modeler. Several test cases applying different morphological acceleration factors have been performed during the validation process. The results of two of these tests are presented in Sections 3.2.4 and 3.3.1.

Expressions are also included that limit the erosion due to suspended and bedload if the quantity of sediment at the bed approaches zero (i.e., a fixed layer is approached). These expressions are formulated so that the continuity of sediment mass in the model is not violated.

2.5.5. Feedback to hydrodynamics

The depth to the bed in water level and velocity points is (optionally) also updated every half time step. This takes into account the total change in mass of all sediment fractions present in a computational cell. At this stage of development, all sediment fractions are assumed independent and instantly mixed. This simple bottom model is perfectly adequate for the simulations presented in this paper, which only use one sediment fraction. An improved bed model is the subject of ongoing development efforts and more advanced bottom updating models are available in research versions of the code (e.g., as implemented by van Ledden and Wang, 2001).

To ensure stability of the morphological updating procedure, it is important to ensure a one-to-one coupling between bottom elevation changes and changes in the bed shear stress used for bedload transport and sediment source and sink terms. This is achieved by using a combination of upwind and downwind techniques as follows:

- Depth in water level points is updated based on the changed mass of sediment in each control volume.
- Depth in velocity points is taken from *upwind* water level points.

- Bed shear stress in water level points (used for computing bedload sediment transport and suspended sediment source and sink terms) is taken from *downwind* velocity points.
- Bedload transport applied at velocity points is taken from *upwind* water level points.

3. Validation tests

The tests performed to validate the sediment version of DELFT3D-FLOW can be divided into three categories: (1) simulations for which an analytical solution exists; (2) simulations of physical experiments and prototype situations that have reliable initial, boundary, and final conditions; and (3) simulations of situations where the results can only be compared with theoretical considerations and results produced by other computer models.

3.1. Comparison with analytical solutions

3.1.1. Equilibrium conditions

Under equilibrium (i.e., stationary and uniform) conditions, the advection diffusion equation reduces to

$$cw_s + D_V \frac{dc}{dz} = 0 \tag{46}$$

Under the assumptions of a constant sediment fall velocity and a parabolic sediment mixing profile, this equation has the solution

$$\frac{c}{c_a} = \left[\frac{a(h-z)}{z(h-a)}\right]^{\lambda} \tag{47}$$

where the suspension number, $\lambda=((w_s)/(\beta\kappa u_*))$.

This is commonly referred to as the "Rouse" sediment concentration profile. A series of tests were performed simulating the suspended sediment transport in a very long (8 km) straight flume with a constant water depth of 5.0 m. The depth-averaged velocity in the flume was 2.0 m/s. Fig. 3 shows the sediment concentrations calculated 6 km from the upstream boundary where clear water enters the flume. The results of five simulations performed using differing numbers of (logarithmically spaced) layers, and different turbulence closure models (TCMs) are presented, superimposed on the analytical Rouse profile. It is clear that, under equilibrium conditions, the computed sediment concentrations are not sensitive to either the number of layers or the chosen TCM, and that all computed results lie close to the analytical Rouse profile.

3.1.2. Suspended sediment transport development

Another interesting case, for which an analytical approximation exists, is the development of suspended sediment transport at the upstream end of a channel with an initially clear flow. In this case, the flow pattern is stationary; however, the suspended sediment transport rate increases with distance down the channel until equilibrium conditions are achieved. This situation was simulated using the DELFT3D-FLOW module and the results compared with the analytical solution of Hjelmfelt and Lenau (1970). The simulation parameters were

$$h = 1.00\ \text{m}, \bar{U} = 1.5\ \text{m/s}, C = 47\ \text{m}^{0.5}\text{s}^{-1},$$
$$a = 0.05\ \text{m}$$

The simulated flume consisted of 120 1-m grid cells in the longitudinal direction and 50 logarithmically spaced layers in the vertical direction. The simulations were performed using the algebraic turbulence closure model. The density effects of the suspended sediment were neglected, and a computational time step of 1.5 s was used. Sediment transport, but not morphological change, was allowed to occur during the simulation. Three simulations were performed with median sediment diameters of 184, 130.5, and 67.5 μm, respectively. These sediment sizes were chosen to produce dimensionless suspension number, λ, values of 0.5, 0.3, and 0.1 for the three simulations. This allowed direct comparison with the analytical results published by Hjelmfelt and Lenau.

Fig. 4 is a vertical longitudinal slice through the first simulation (λ=0.5) and shows contours of equal sediment concentration. In this plot, all variables are nondimensionalized to compare with the analytical

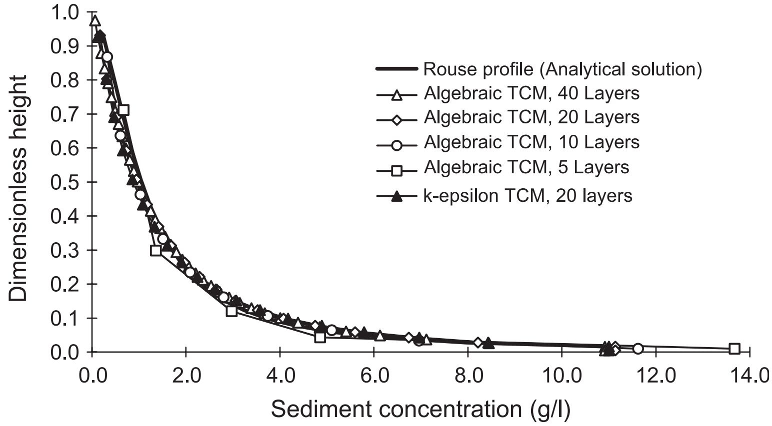

Fig. 3. Equilibrium sediment concentration profiles computed 6 km down a long flume showing the effect of varying layer spacing and choice of turbulence closure model (TCM).

results. The dimensionless variables used in the plot are defined as follows:

$$\lambda = \frac{w_s}{\beta \kappa u_*},\ X = \frac{\beta \kappa u_* x}{\bar{U}}\ h,\ Z = \frac{z}{h},\ C = \frac{c}{c_a},$$

and $A = \dfrac{a}{h}$

Fig. 4 shows that the simulation results reproduce the analytical solution well, although suspended sediment concentrations are overestimated slightly (less than 10%) as equilibrium conditions are approached toward the downstream end of the flume. Further investigation shows that the majority of this error can be attributed to the first-order upwind sediment settling scheme used in the DELFT3D model. This scheme is retained, however, as we consider that its excellent stability in a wide range of flow conditions more than compen-

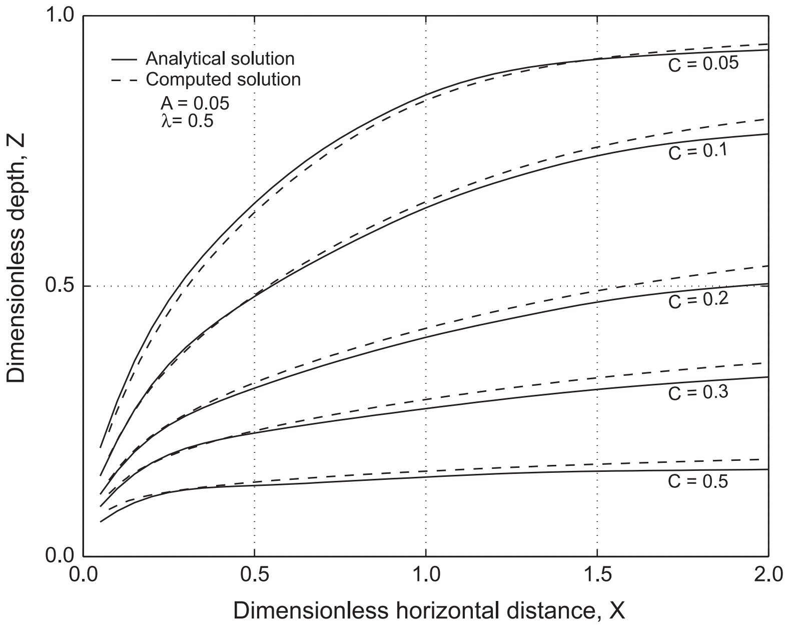

Fig. 4. Contours of equal sediment concentration along a flume showing the adaptation of the suspended sediment concentration from an initially clear flow (after Hjelmfelt and Lenau, 1970).

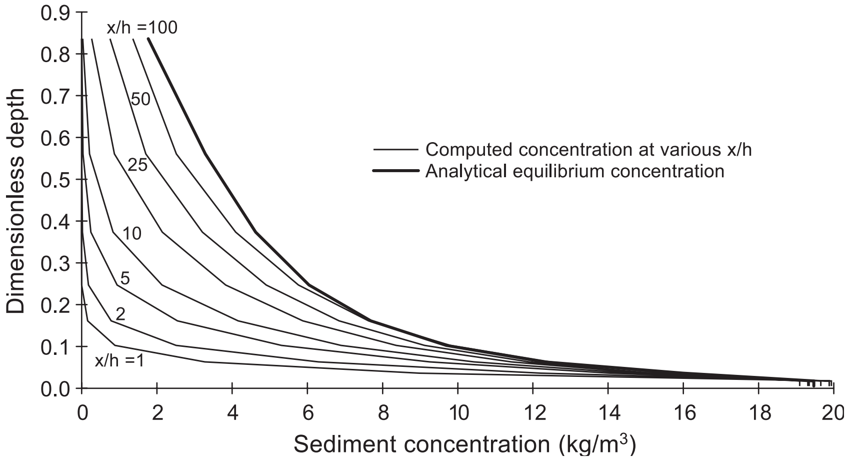

Fig. 5. Suspended sediment concentration profiles at various distances along a flume showing the progressive development of an equilibrium sediment concentration profile.

sates for the slight overestimation of sediment concentrations that it produces.

Fig. 5 illustrates the gradual development of the sediment concentration profile along the length of one DELFT3D model simulation. It can be seen that the profile develops smoothly, and that equilibrium conditions have still not been reached by a distance of x/h=100.

Fig. 6 shows a longitudinal profile of the depth-averaged suspended sediment concentration computed in three simulations using different sediment grain sizes. Again, the computed results compare well with

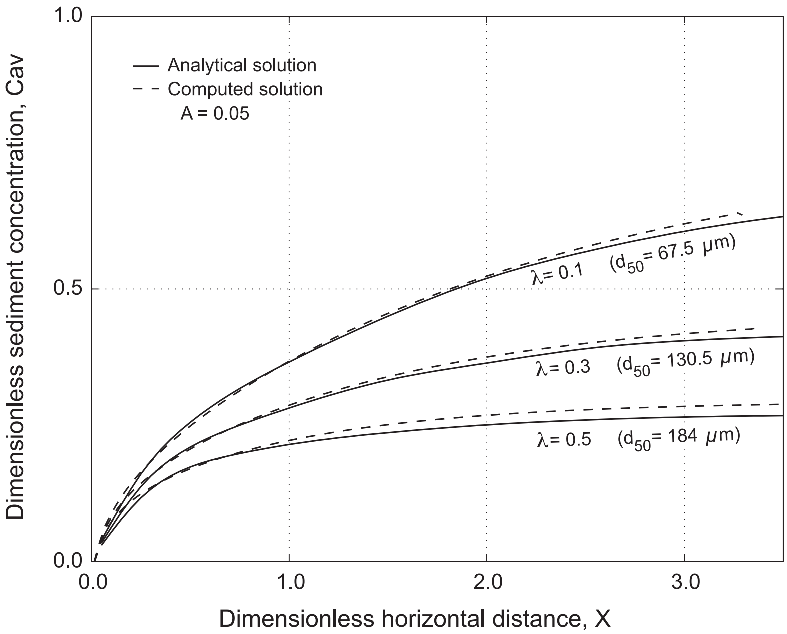

Fig. 6. Development of the depth-averaged suspended sediment concentration along a flume for three different sediment sizes (after Hjelmfelt and Lenau, 1970).

the analytical solution of Hjelmfelt and Lenau. The simulations were repeated using just six σ layers in the vertical and the results were found to be very similar (maximum error of 16% compared to the analytical solution).

3.1.3. Equilibrium slope of a straight flume

In this experiment, a relatively short straight flume with a movable bed is simulated. At the upstream boundary, a constant-discharge boundary condition is applied and the flow enters the flume carrying the local equilibrium suspended sediment concentration profile. At the downstream end of the flume, a constant water level is specified. As the bed of the flume is initially horizontal, an accelerating flow is created. This in turn causes an increasing sediment transport rate along the length of the flume, and erosion of the bed. This process continues until the bed of the flume matches the slope of the water surface and the process becomes stationary; equilibrium conditions have been achieved. Fig. 7 shows the profile of the bed of the flume at four times during the simulation. It can be seen that a stable solution is reached after approximately 30 h and that, after a small (2 mm) adaptation near the upstream boundary, the equilibrium bottom profile forms a straight line at a constant slope. Simple calculations confirm that the slope of the bed is very close to the theoretical slope of the water surface given the specified discharge and bed roughness.

3.1.4. Settling basin

The opposite case to the development of a sediment concentration profile is the falling of sediment out of suspension when the energy of a flow decreases. Fig. 8 shows the result of a simulation of a perfectly still settling basin containing water with an initial uniform sediment concentration of 2 kg/m^3.

In theory (neglecting background molecular diffusion), all the sediment should fall to the bottom and accumulate in the time taken for a single particle to fall from the water surface to the bed. Fig. 8 shows the result of just such a simulation. In this case, the water is 5-m deep and the sediment settling velocity is 0.0257 m/s. In theory, all sediment should accumulate in 3.25 min. It can be seen that DELFT3D approximates the theoretical solution rather well, especially when the computational time step is reduced. Several configurations with different layer spacings were tested and little sensitivity was discovered. In all tests, the total quantity of sediment available in the flow does accumulate at the bed; continuity of sediment is preserved.

3.2. Comparison with physical models and prototype measurements

3.2.1. Trench migration experiment

In this experiment, water flows across a steep-sided trench cut in the sand bed of a flume. The water reaches the upstream edge of the trench carrying the

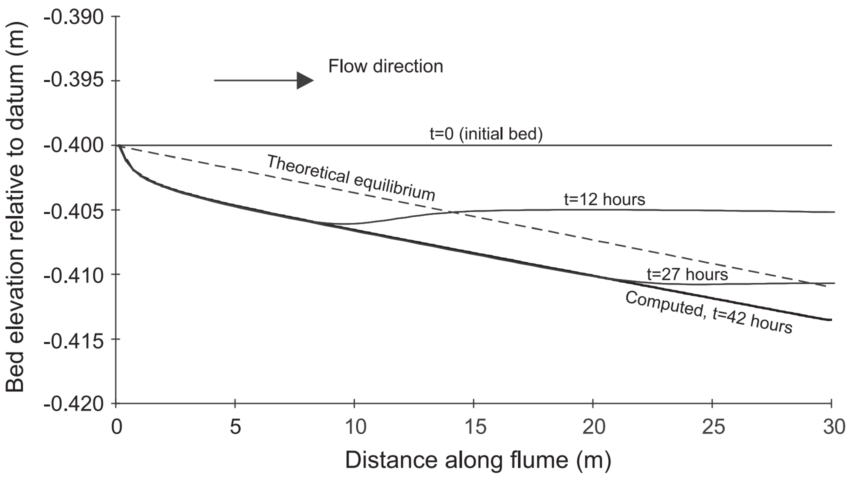

Fig. 7. Longitudinal profile of the bed of a simulated flume at four times during a morphological simulation, showing the development of an equilibrium slope from an initially horizontal bed.

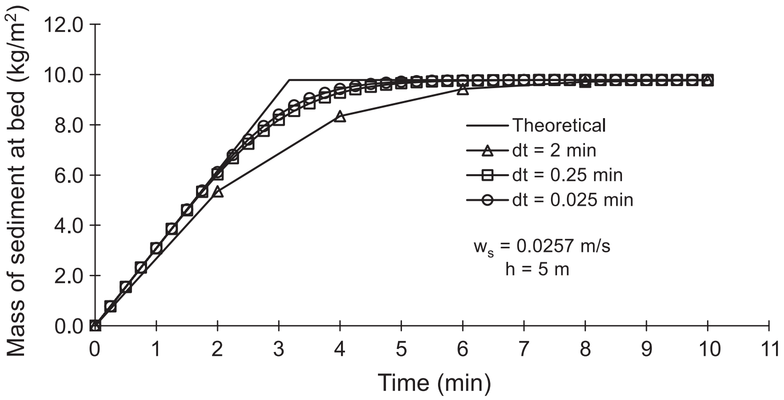

Fig. 8. Results of the settling basin test showing accumulation of initially suspended sediment at the bed. Three simulations show the influence of the computational time step on the computed result.

equilibrium suspended sediment concentration profile. As the flow decelerates over the deeper trench, some sediment is deposited. Sediment is then picked back up by the accelerating flow at the downstream edge of the trench. Due to the spatial difference between the areas of deposition and erosion, the trench appears to migrate downstream. Fig. 9 shows the initial situation before the trench starts to deform. Both the results of measurements carried out by van Rijn (1987) and the computed results of DELFT3D-FLOW are presented. The significant changes in both flow velocity and sediment concentration profiles, measured as the flow crosses the trench, are well represented in the DELFT3D simulation.

Fig. 10 shows the measured and computed position of the trench after 15 h. It can be seen that the trench has been reduced to approximately one-half of its initial depth, and has migrated about 3 m downstream. The computed result is in very good agreement with the measurements. All computational tuning parameters were left at their default values.

3.2.2. Curved flume experiment

In this experiment, another flume test was simulated. In this case, the flume began with a straight inflow section 7-m long followed by a bend of 140° with a radius of curvature of 12 m and a straight outflow section 11-m long. The width of the flume was 1.5 m. The flume had a mobile sand bed and a sand pump was used to recirculate the sand deposited at the downstream end of the flume. The flume was run at a constant discharge for approximately 2 weeks until an equilibrium state was reached. Over a period of 3 days, 25 sets of bed-level readings were taken at 10 points across each of 45 cross-sections. The number of repeated readings was judged to be

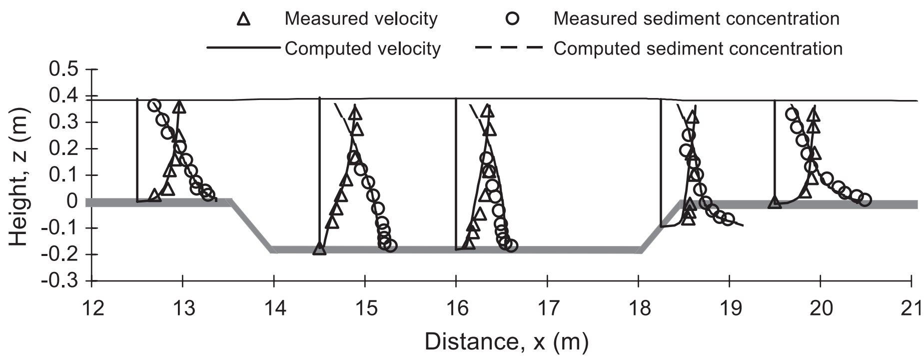

Fig. 9. Measured and computed velocity and sediment concentration profiles across a trench in a flume before significant morphological development takes place (after van Rijn, 1987).

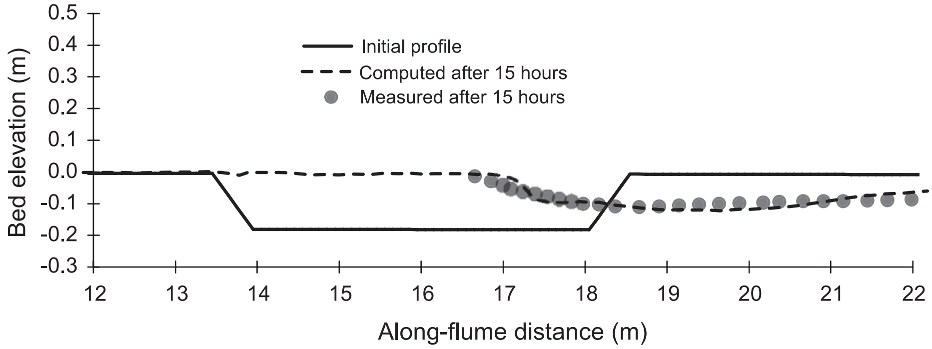

Fig. 10. Measured and computed trench profile after 15 h (after van Rijn, 1987).

sufficient to remove the effects of slowly propagating bed forms and to provide a reliable estimate of the time-averaged bed level at each point (Fig. 11).

The important parameters governing the experiment were as follows: Q=0.047 m^3/s, $\bar{h}$=0.08 m, $\bar{u}$=0.39 m/s, I=2.36×10^{-3}, C=28.4 m$^{0.5}$/s, and D_{50}=450 μm where I is the average longitudinal slope of both the water surface and bed. For a detailed description of the model features and operation, reference is made to Struiksma (1983).

The left panel of Fig. 11 shows the equilibrium water depths measured in the experiment. The measurements clearly show the effect of the 3D spiral flow in the bend on the bathymetry, as well as a less distinct oscillation caused by the entire depth-averaged flow "bouncing" from one wall of the flume to the other, around the bend, and continuing downstream. The experiment was simulated using the online sediment version of DELFT3D using a curvilinear grid consisting of 10×93 grid cells and 10 σ-

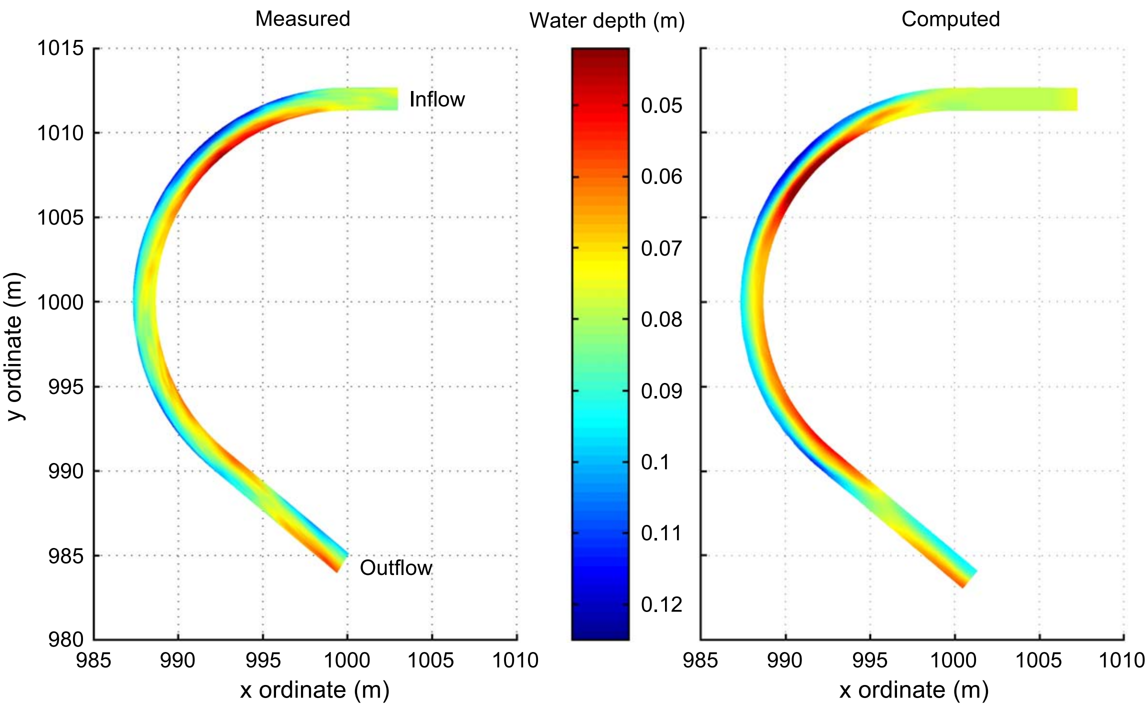

Fig. 11. Measured and computed equilibrium water depths in a curved flume (after Struiksma, 1983).

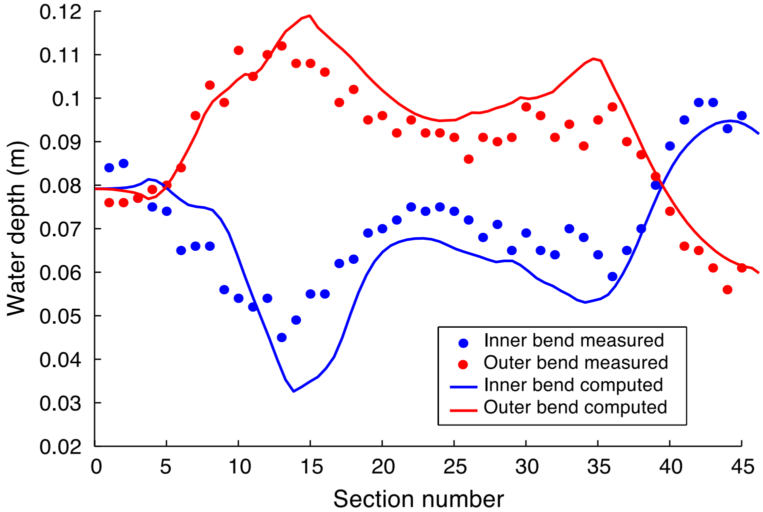

Fig. 12. Longitudinal profiles of measured and computed equilibrium bed levels 0.225 m from each side wall of a curved flume.

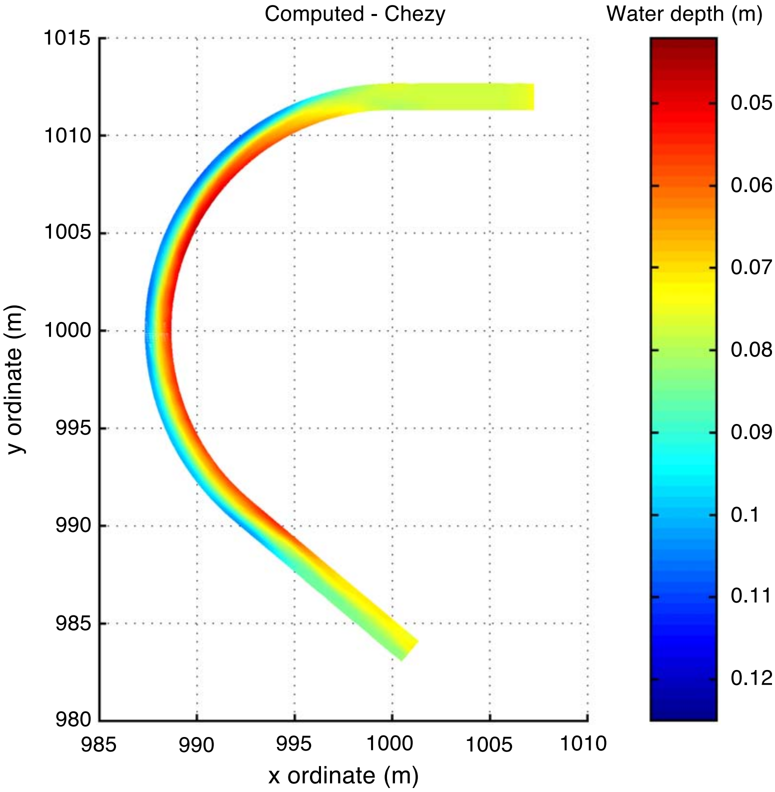

Fig. 13. Equilibrium water depths in a curved flume computed using a Chezy roughness coefficient.

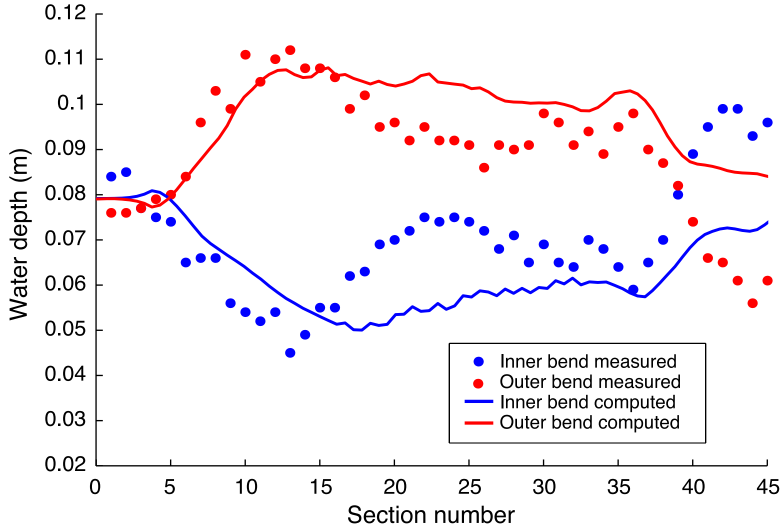

Fig. 14. Longitudinal profiles of measured and computed equilibrium bed levels 0.225 m from each sidewall of a curved flume. Computation uses a Chezy roughness coefficient.

layers in the vertical. The numerical model was run using the geometry and parameters described above, using bedload sediment transport only, until the bathymetry became reasonably stable (33 morphological hours). The results can be seen in the right panel of Figs. 11 and 12.

Again, the computed result is favorably close to the measured bathymetry. We emphasize that this result was achieved with all sediment and flow parameters set at default values with the three following exceptions: (1) the horizontal fluid viscosity was reduced to a constant value of 0.001 m^2/s to reflect the rather fine computational grid, (2) the transverse bed-slope effect factor was increased from 1.5 to 2.0, and (3) the bed roughness was specified as a constant roughness height of 0.025 m, rather than use the Chezy value of 28.4 $m^{0.5}/s$ specified in the description of the experiment. We found that, in this case, it is essential to specify a constant roughness height as the depth changes significantly across the flume. When the Chezy roughness formulation is used, the roughness height becomes a function of the water depth, thereby introducing a significant variation in roughness across the flume. In this case, specifying a Chezy roughness value appears to have a strong damping effect on the bathymetry—not in line with the experimental results. The bathymetry and long sections for the same simulation performed using the Chezy roughness coefficient are presented in Figs. 13 and 14.

3.2.3. Wave and current flume experiment

This experiment conducted by Dekker and Jacobs (2000) in a 45-m-long wave flume investigated the velocity and sediment concentration profiles produced by three combinations of waves and currents acting

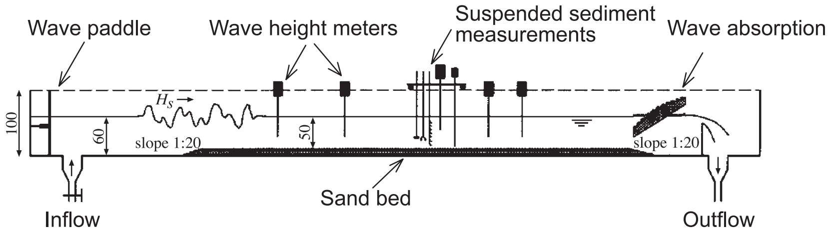

Fig. 15. Arrangement of wave and current flume experiment (after Dekker and Jacobs, 2000).

over a sand bed (D_{50}=165 μm). All experiments were performed using random waves (H_s=15 cm). The strength of the current, which was always in the same direction as the waves, was varied from one experiment to the next. The layout of the flume used in their experiment is reproduced in Fig. 15; the water depths are indicated in centimeters. The sediment measurements were made 14 m downstream from the start of the mobile sand bed.

The results of three of Dekker and Jacobs' experiments and the corresponding computer simulations using the $k-\varepsilon$ TCM and 20 σ-layers are presented in Figs. 16–18. The results using the algebraic TCM were very similar. Fig. 16 shows the profiles recorded for the wave-only (no net current) experiment. Fig. 17 shows the results including a following current of 0.26 m/s. In Fig. 18, the velocity of the following current was increased to 0.40 m/s. The difference between the velocity profiles measured in each of the experiments is clearly visible when comparing the three sets of figures. In Fig. 16, the influence of the wave streaming can clearly be seen in the near-bed region. The computed sediment concentration profiles agree remarkably well with the measurements under all the wave and current combinations tested. We note that these numerical simulations were performed with all tuning parameters left at their default settings.

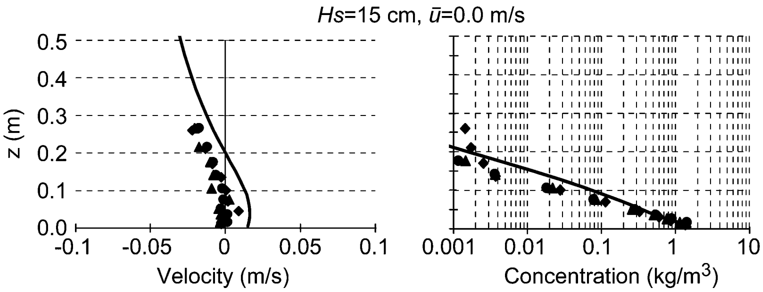

Fig. 16. Measured and computed velocity and sediment concentration profiles for waves with no net current.

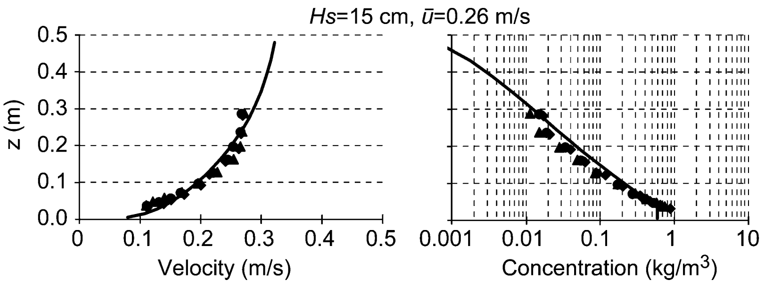

Fig. 17. Measured and computed velocity and sediment concentration profiles for waves with a moderate following current.

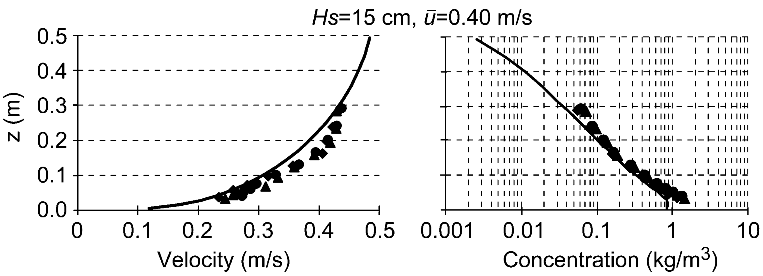

Fig. 18. Measured and computed velocity and sediment concentration profiles for waves with a stronger following current.

3.2.4. IJmuiden harbor morphological development

As a more severe real-life test case, we chose the evolution of the sea bed and adjacent coast at IJmuiden. The breakwaters of IJmuiden, the seaport of Amsterdam (see Fig. 19), were extended by approximately 2500 m during the period 1962–1968. Since then, a large scour hole has developed near the tip of the longest, southern, breakwater and the coastline has accreted more than 500 m, especially on the southern side of the harbor. Further away from the harbor the coast has suffered erosion.

Regular bathymetric surveys of the area have been performed and dredging data have been collected. Roelvink et al. (1998), compiled, digitized where necessary, and tailored these data for model validation. Data have been collected over a period of 28 years; however, in this paper, we focus on the first 8 years of morphological development, from 1968 to 1976. The shore-parallel tidal motion in the area is well documented and several operational models exist that can be used to generate boundary conditions for a detailed model of the vicinity of the harbor. Directional wave data are available from nearby stations in approximately 20 m of water depth.

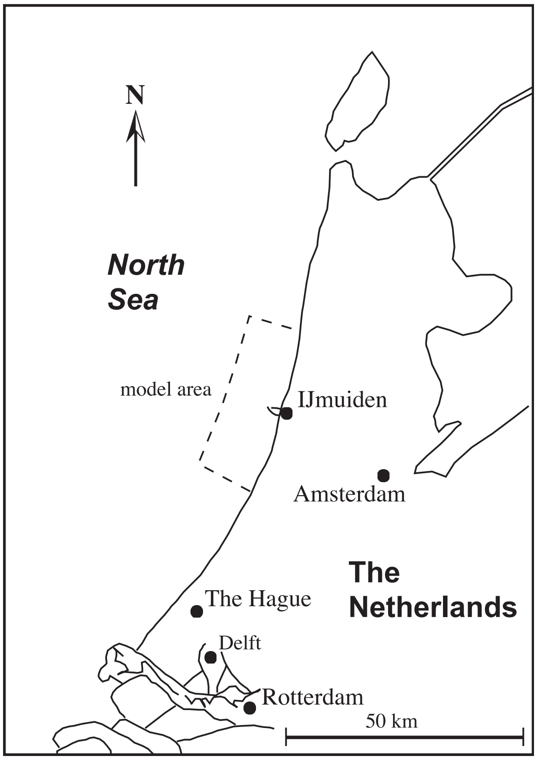

Fig. 19. The location of IJmuiden on the Dutch coast.

Roelvink et al. (1998) compared several model simulations. These simulations used the 2DH (offline) mode of the DELFT3D model system (DELFT2D-MOR) and transport formulations by Bijker (1971), and were compared with a simplified transport update scheme. Qualitatively, a reasonable agreement was found for the development of the scour hole and deposition zones north and south of the breakwaters. However, the deposition zones were too pronounced compared to the measurements.

During the period of 1968–1976, the morphological developments in the area around the breakwater tips (water depths of 15–20 m) and in the nearshore areas were almost unconnected; the first was very much tide dominated while the second was mainly wave dominated. This allows us to take a stepwise approach to testing the results of the present model.

The DELFT3D-FLOW model was set up both in 2DH and 3D mode. First, 2DH simulations were performed to test the effect of the morphological factor. Then, the model was extended to 3D and simulations were performed both with and without waves. Finally, a simulation with a different bed roughness formulation was made to check the sensitivity of the model to this important parameter. Table 1 gives an overview of the runs made.

A curvilinear grid was constructed with a good (approximately 100 m) resolution near the harbor entrance and near the coast, but gradually coarsening toward the model boundaries, which were located some 10–15 km from the harbor. A single representative tide was selected based on initial transport computations over a spring-neap cycle. The selected tide had an amplitude of 1.1 times the average tidal amplitude.

Table 1
Morphological simulations performed for IJmuiden breakwater extension

Run no.	Dimensions	Morphological factor	Waves	Roughness	Period
1	2DH	20	No	n=0.028	1968–1976
2	2DH	100	No	n=0.028	1968–1976
3	3D	100	No	n=0.028	1968–1976
4	3D	100	Yes	n=0.028	1968–1971
5	3D	100	Yes	C=60	1968–1971

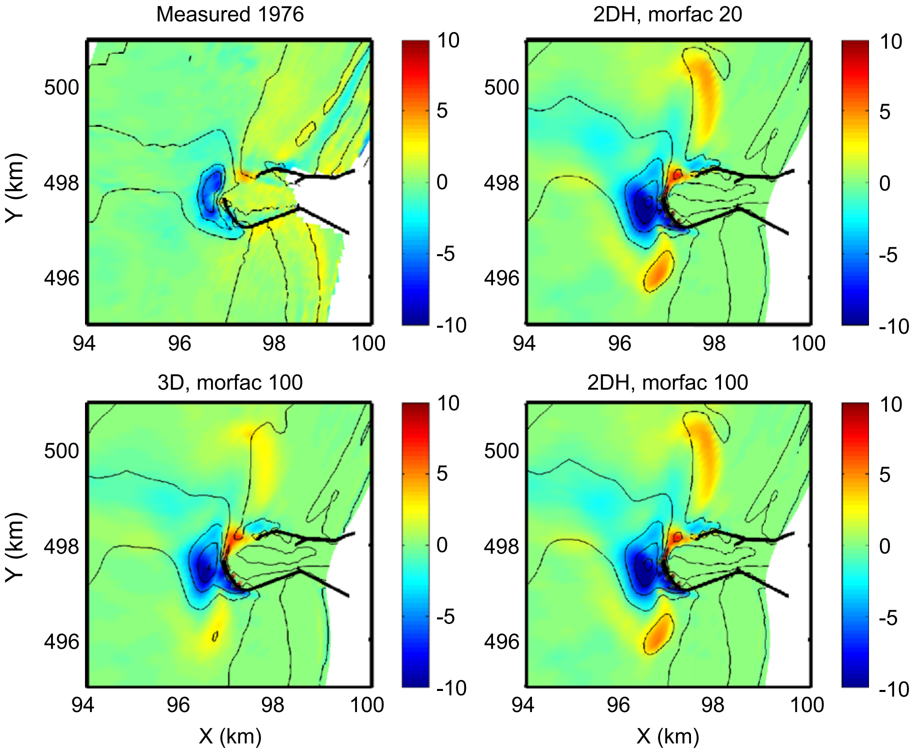

Fig. 20. IJmuiden, measured and computed sedimentation (red) and erosion (blue) patterns for 2DH and 3D morphological simulations of the period 1968–1976 (no waves).

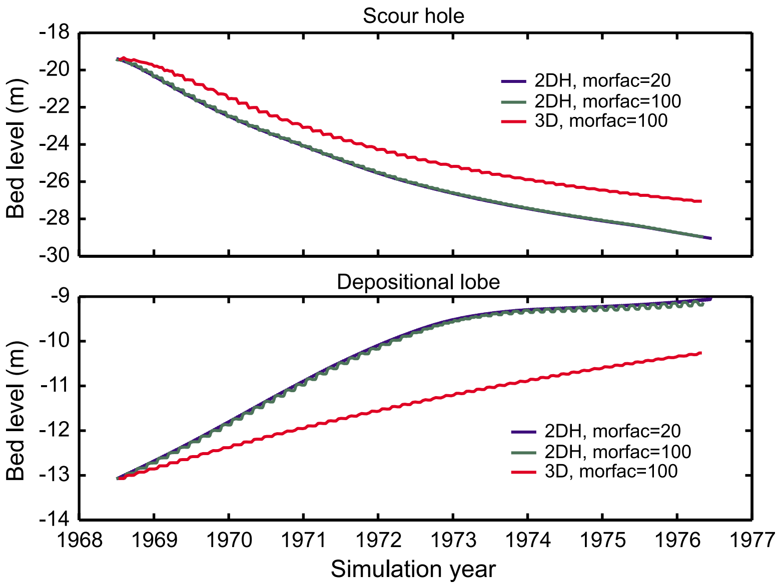

Fig. 21. IJmuiden, time evolution of bed elevation for a point in the scour hole (upper) and a point in the deposition area (lower).

All runs were made with a time step of 2 min. To simulate 8 years of morphological change, the run with a morphological factor of 20 required the flow computation last for 280 tidal cycles. With a morphological factor of 100, only 56 tidal cycles had to be simulated. In the 3D case, eight nonequidistant layers were chosen and the algebraic TCM was applied.

In Fig. 20, the morphological changes computed in the first three runs are compared with the measured sedimentation and erosion. A comparison between the runs with different morphological factors shows no discernible difference. A comparison of these two simulations is presented in more detail in Fig. 21, which shows the time evolution of the bed elevation for two points, one located in the scour hole and the other in the southern deposition lobe. It is clear that the morphological changes within a tidal cycle, even scaled up by a factor of 100, are still small compared to the water depth and the longer-term morphological trend.

The 2DH simulation results are very similar to those presented by Roelvink et al. (1998), although the location of the scour hole has improved as the thin dams applied in the present model better fit the actual breakwater alignment. The computed erosion and deposition pattern is still too strong, however, resulting in too much erosion and strongly overestimated deposition lobes. For the 3D run, this situation is much improved. The scour hole becomes less deep and the depositional areas are much less pronounced. However, in all simulations, it is clear that very little happens in the nearshore area, contrary to the measurements. It is likely that this is due to the lack of wave-driven currents and sediment transport.

For the runs including waves, a schematized time series of wave conditions was created. The basis for this was the wave climate recorded at the Euro Platform wave buoy over the period 1979–2001. The total wave climate was binned in 2-m H_s, 30° direction, wave classes. For each of these classes, a weighted average H_s and mean direction and wave period were computed. The expected annual occurrence duration of each wave class was divided by 100

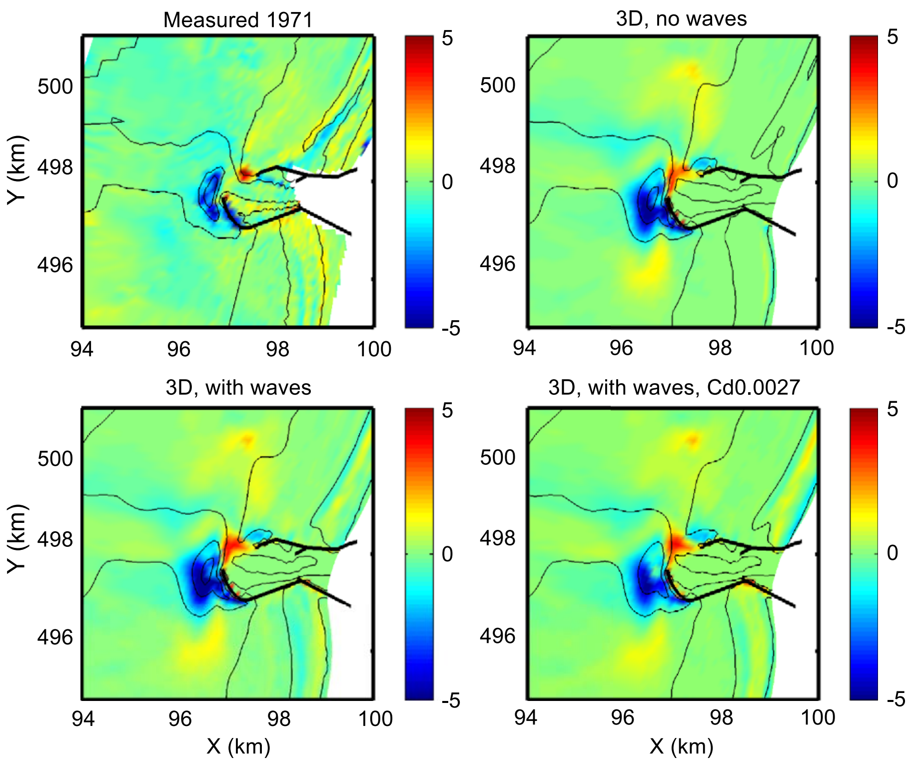

Fig. 22. IJmuiden, measured and computed sedimentation (red) and erosion (blue) patterns for 3D morphological simulations of the period 1968–1971.

(reflecting the morphological acceleration factor) and the wave classes were arranged one after the other in random order to make a 1-year time series. This time series was repeated for each year of the morphological simulations.

The set-up of the simulation was simple: The flow model including sediment transport and morphological changes were run for 1 h (100 h of morphological change), then the waves were updated using the updated bathymetry and water levels from the flow model, after which the flow model ran with updated waves. This cycle was repeated for 56 tidal cycles. The SWAN model was used to compute the waves on a curvilinear grid identical to the flow grid except for extensions at the southern and northern ends. As these runs are somewhat more demanding, they were carried out for only 3 years. The morphological evolution was smooth, however, and longer simulations are possible.

In Fig. 22, the results are compared with the observed erosion and sedimentation over the period 1968–1971. Run no. 4 (lower-left panel) had the same roughness settings as the other runs, viz. a Manning coefficient of 0.028, which was adopted from the regional model in which this model was nested. Clearly, much more is happening in the nearshore than in the runs without waves, but it still rather underestimates the observed accretion near the breakwaters. The Manning coefficient used is fairly high, but leads to an especially strong increase in bed friction in the shallow water near the coast. This leads to a sharp reduction in longshore velocity and sediment transport. In the last run, a constant Cd value of 0.0027 was applied (following the findings of Ruessink et al., 2001). This setting gives similar roughness in deep water but much less in shallow water. The results of this simulation (lower-right panel) show a marked increase in transport near the coast and much stronger deposition beside the southern breakwater, in line with the observations. The change in roughness coefficient, however, had a marked impact on the depth of the predicted erosion hole, which is now rather shallower than observed. This observed sensitivity of the predicted morphology to selected bed roughness coefficient clearly indicates an area requiring further research to develop a reliable predictor of bed roughness under the combined influence of waves and current.

3.3. Comparison with other numerical models

3.3.1. Hump test

This test checks a theoretical test problem previously discussed by de Vriend (1987). An east–west oriented rectangular channel 10-m deep, 10-km wide, and 20-km long was subjected to eastward flow with a velocity of 1 m/s. The bed of the channel consists of sand (d_{50}=200 μm) and contains a Gaussian hump with a radius of 1 km and initial height of 5 m (see the top two panels of Fig. 23).

In the center-left panel of Fig. 23, we see the evolution of the hump according to a standard 2DH DELFT2D-MOR simulation, using Van Rijn bedload and suspended-load transport for a duration of 200 days. Typical for this type of evolution is that the top of the hump moves in the direction of the flow, but two lobes extend obliquely at the same time. On either side of the hump, and in front of it, there are regions of erosion.

The remaining panels of Fig. 23 present the results of three 3D simulations using the online sediment version of DELFT3D-FLOW. It is clear that the 3D results are qualitatively similar to those of the 2DH simulation. However, the development of the lobes is less pronounced in the 3D simulations and the bathymetry predicted after 200 days is somewhat smoother in the 3D case. Comparison of the bed-shear stress distributions for the 2DH and 3D simulations at the start of the morphological changes shows that the gradients in bed-shear stress are significantly reduced in the 3D simulation due to deformation of the logarithmic velocity profile. We expect that this smoother distribution of bed-shear stress causes the smoother development of the bathymetry in the 3D simulation.

Comparison of the results of the 3D simulations also serves as another useful test of the morphological acceleration factor included in DELFT3D-FLOW. Over these simulations, the morphological acceleration factor increases by a factor of 25 (thereby decreasing the required hydrodynamic simulation duration by the same factor). Little difference can be seen in the resulting bathymetry after 200 morphological days. Therefore, we can confidently state that the use of even a rather high morphological acceleration factor has little impact on the development of the morphology in this situation. We stress,

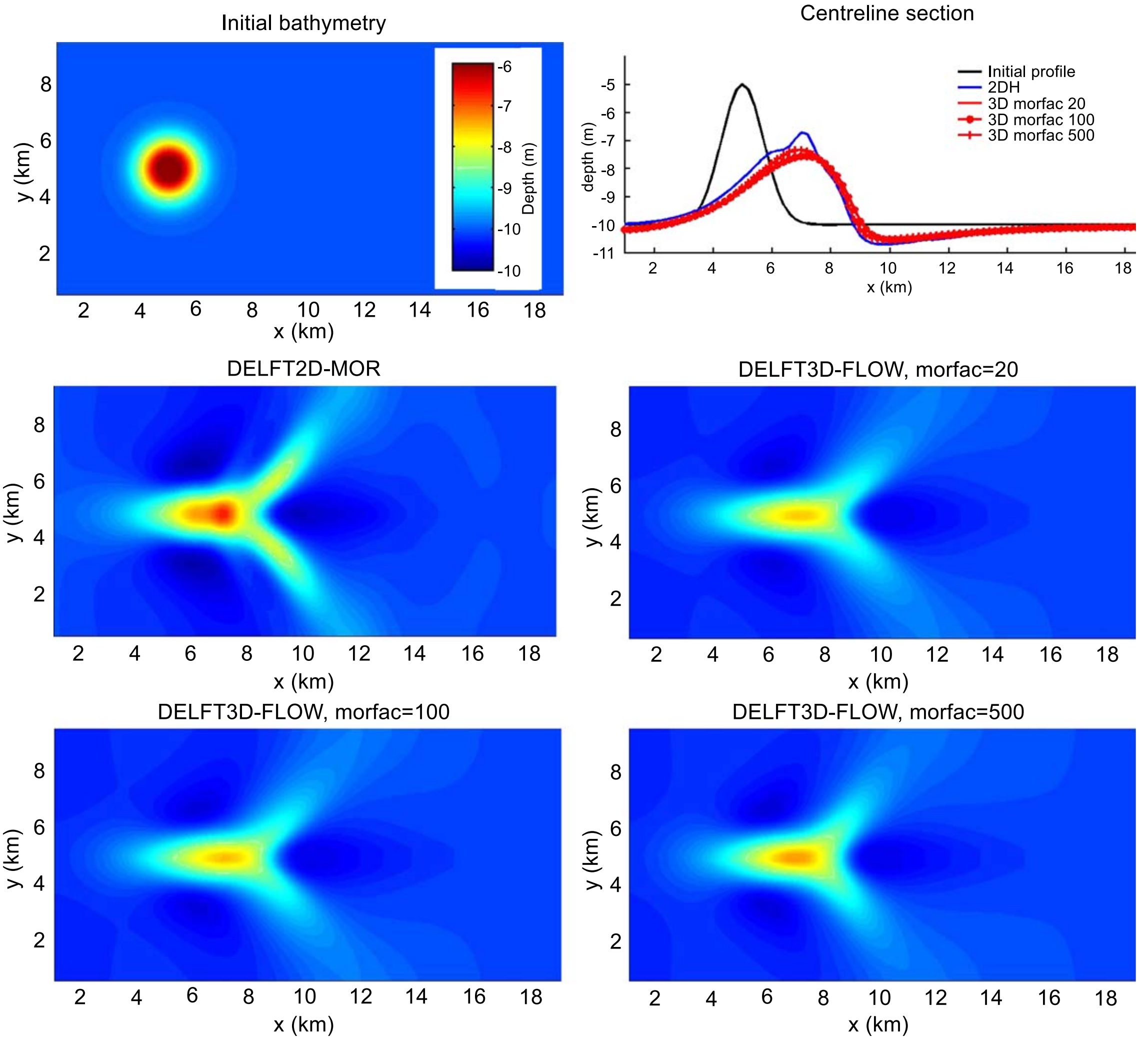

Fig. 23. A rectangular channel containing a Gaussian hump is subjected to an east to west flow for 200 days. Top-left panel shows initial bathymetry; top-right panel shows centerline sections through the hump initially; and after each simulation. The remaining panels show aerial views of the deformed bathymetry predicted by four different model simulations.

however, that appropriate morphological acceleration factors must be chosen and tested on a case-by-case basis.

3.3.2. Offshore breakwater case

3.3.2.1. Introduction. As a more complex test of the combined modeling of waves, currents and morphological changes in 3D, we elected to use the offshore breakwater test case reported in Nicholson et al. (1997). Nicholson et al. used this test case to compare five different 2DH morphodynamic models, including the standard version of DELFT2D-MOR.

The test geometry consists of a long straight coastline with a planar sloping beach. Offshore from the beach lies a shore-parallel surface-piercing impermeable breakwater. The only driving force in the test is provided by the incoming waves, which enter perpendicular to the coast. Longshore gradients in wave set-up drive a double circulation pattern in the nearshore flow that tends to bring sand into the sheltered area behind the breakwater. This leads to the formation of a

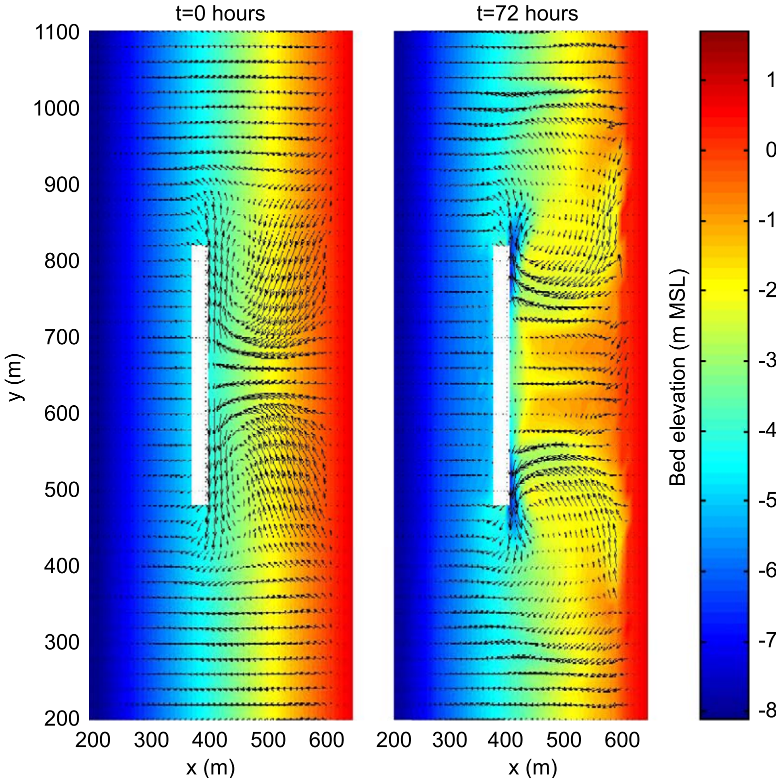

Fig. 24. Overall view of initial (left panel) and final (right panel) bathymetry and near-bed flow fields computed for an offshore breakwater subject to shore-perpendicular waves.

tombolo or salient. The main characteristics of this test case are: beach slope=1:50, breakwater length=300 m, breakwater axis-to-shore distance=220 m, sediment d_{50}=250 m, incident RMS wave height=2.0 m, and peak wave period=8.0 s.

3.3.2.2. Model set-up. The model domain was chosen to be 1300-m longshore by 700-m cross-shore. A rectangular computational grid with a 20 m (longshore) by 10 m (cross-shore) resolution was used for the flow model. The cross-shore resolution was increased to 5 m for the wave model. In the vertical, the flow model used six σ-layers with layer thickness ranging from 5% to 35% of the water depth. Thinner layers were used near the surface and the bed. The algebraic TCM was used to compute 3D turbulence.

The time step for the flow model was set at 6 s and a morphological acceleration factor of 24 was used. This meant that 1 h of flow computation represented one full day of morphological change. Because the waves were perpendicular to the beach, all flow model boundaries could be closed boundaries. For the wave model, the side boundaries were chosen to be reflecting to minimize disturbances. The wave computation was updated after every 10 flow time steps (1 min in flow, or 24 min of morphological time).

3.3.2.3. Results. The initial bathymetry and near-bed flow field are shown in the left panel of Fig. 24. The expected pattern of two circulation cells rotating in opposite directions, driven by wave set-up gradients is clearly visible. A closer view of the initial situation at one end of the breakwater is shown in the left panel of Fig. 25. This figure also shows the current vectors at the water surface, which are clearly different from the flow near the bed. This is due to (1) helical flow, which pushes the upper-layer velocities outward; and (2) undertow, which gives a seaward component near the bed in the surf zone.

The right panels of Figs. 24 and 25 show the bathymetry and corresponding flow patterns after 72 h of morphological change have occurred. The model is clearly demonstrating a tendency to accumulate sediment behind the breakwater, with the salient reaching from the shoreline almost out to the breakwater. The crest of the salient has reached a level of one meter below the still water level, which is likely to be as high as it can grow in the absence of a tidal range. Significant erosion occurs near the beach on either side of the breakwater and a deep scour channel is formed inshore of the tips of the breakwater.

At first sight, the results are quite similar to the results of the 2DH models given in Nicholson et al. (1997). A difference, however, is that the accretion behind the breakwater occurs at the expense of stronger erosion of the beach at the edges of the lee zone, due to undertow. In addition, the scour holes at the breakwater tips develop more strongly, probably due to the helical flow that diverts the near-bed flow away from the breakwater.

We conclude that, although further analysis and quantitative comparison of model results are desirable, these results are a promising first step for a fully 3D process-based morphological model. The model has shown the ability to combine much of our present state-of-the-art knowledge of waves, flow, and sediment transport to produce smooth and, at least, qualitatively realistic morphological changes.

4. Discussion

The validation cases presented here show that the online sediment version of DELFT3D-FLOW is capable of simulating many of the processes that are relevant in coastal environments, both separately and in combination. This has been achieved by adding bedload and suspended-load sediment transport and morphological change to a 3D hydrodynamic flow model. The advantages of this approach are: (1) complex 3D flow effects can be automatically included in a morphological simulation; (2) it is simple and efficient to use the standard implicit transport solver in the flow model to compute the transport of suspended sediment; (3) large communication files can be avoided; and (4) the density effects of suspended sediment concentrations on the flow can be taken into account, although the benefits of this last point have not been illustrated in this paper.

The model has been validated across a range of processes and process interactions. The validation studies reported in this paper have demonstrated the model's response to the following processes: (1) entrainment, transport, and settling of sediment, (2) varying levels of uniform bed shear stress, (3) accelerating and decelerating flow, (4) spiral flow in a bend, (5) bed slope effects, (6) the effects of wave orbital motion on suspended sediment concentration, and (7) the effects of undertow and wave-driven currents.

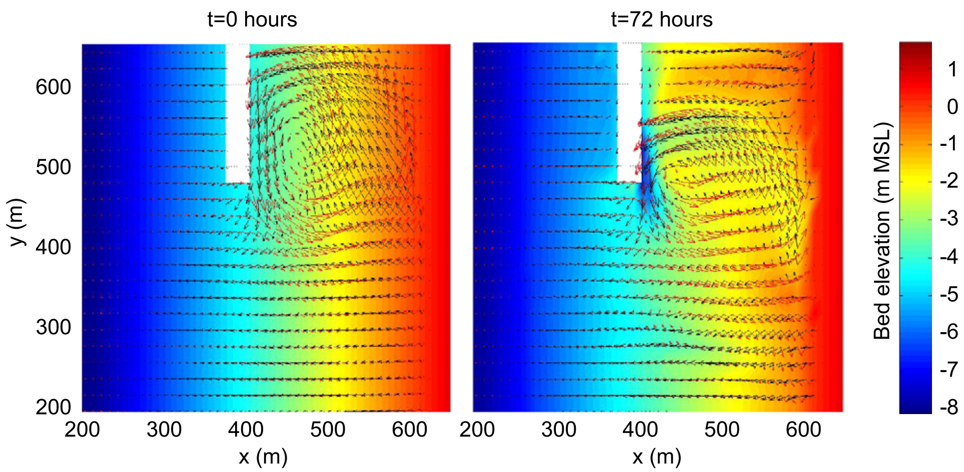

Fig. 25. Detail view of initial (left panel) and final (right panel) bathymetry, near-bed flow field (black arrows) and near surface flow nfield (red arrows).

Although many of the datasets used in the validation of the model originate in the laboratory, the model is efficient enough to be used in the analysis of real-life, prototype-scale situations. The suspended transport, bedload transport, and morphological changes are computed using the same time-step as the flow model, but morphological changes are accelerated by use of a morphological acceleration factor. It has been demonstrated that for simple cases, very high morphological factors can be used without significantly changing the solution. For tidal and wave-driven situations, results have been presented indicating that values in the order of 50–100 are viable. Another factor contributing to the efficiency of this model is the use of σ-layers. With a sensible (smooth, logarithmic) distribution of layer thickness, the concentration vertical can be efficiently resolved. Fewer than 10 layers appear to be required when using an algebraic turbulence model, 10–20 for a k-epsilon model. When combined, these factors allow useful morphological simulation periods to be covered within acceptable run times. This situation can only be expected to improve as increasing computing power continually expands the horizons of simulation duration and resolution.

The fact that any combination of 3D flow processes, including the effects of sediment, can now be included in a morphodynamic simulation opens up a plethora of modeling possibilities. However, a vast amount of work lies ahead in the verification of the model, for even the most common combinations of processes, and in the refinement and extension of the model components. A clear example of the need for further development is provided by two of the tests presented in this paper, which show a marked sensitivity to the chosen bed roughness parameter. It is well known that in reality bed roughness is highly variable both in space and in time. This reality is far more complex than the formulations employed in the present model and is an area that clearly requires both an advancement of the state of the art of our understanding and the parallel development and validation of reliable model formulations.

In view of this, this paper must be seen as a status report of work in progress. The work will be continued on a broad front, and cooperation with persons and institutes worldwide is strongly encouraged. Future efforts will focus on the definition of further test cases, the generation of comprehensive datasets for validation of specific combinations of processes, the refinement and extension of model formulations, and the testing and application of the model.

List of Symbols

a	Reference height for suspended sediment concentration (m)
c	Mass sediment concentration (kg/m^3)
c_a	Mass sediment concentration at reference height a (kg/m^3)
d	Depth to bed from reference datum (positive down) (m)
d_{50}	Median sediment diameter (m)
D_H, D_V	Horizontal and vertical diffusion coefficients (m^2/s)
$D*$	Dimensionless sediment diameter
f	Coriolis coefficient (inertial frequency) (s^{-1})
h	Water depth (m)
H_s	Significant wave height (m)
k	Turbulent kinetic energy (m^2/s^2)
P	Pressure (Pa)
S	Salinity (ppt)
S_b	Bedload sediment transport (kg/m/s)
T	Dimensionless shear stress
T_p	Peak wave period (s)
u, v, w	Eulerian velocity components in Cartesian coordinates (m/s)
U, V	Generalized Lagrangian Mean (GLM) velocity components (m/s)
u_*	Bed shear velocity (m/s)
$\bar{U}, \bar{V}$	Depth-averaged GLM velocity components (m/s)
$\hat{U}_\delta$	Peak orbital velocity at the bed (m/s)
w_s	Sediment fall velocity (m/s)
z	Vertical Cartesian coordinate (m)
β	Ratio of sediment diffusion to fluid diffusion
ε	Dissipation in transport equation for turbulent kinetic energy (m^2/s^3)
κ	Von Karman's constant (=0.41)
ν_H, ν_V	Kinematic viscosity (m^2/s)
ρ	Local fluid density (including salinity, temperature and sediment) (kg/m^3)
ρ_0	Reference density of water (kg/m^3)
ρ_s	Density of solid sediment particles (kg/m^3)

σ Vertical "sigma" coordinate
τ_{bx}, τ_{by} Bed shear stress components (N/m^2)
ω Vertical velocity component in sigma coordinate system (s^{-1})
ζ Water surface elevation above reference datum (m)

References

Andrews, D.G., McIntyre, M.E., 1978. An exact theory of nonlinear waves on a Lagrangian-mean flow. Journal of Fluid Mechanics 89 (4), 609–646.

Bagnold, R.A., 1966. An Approach to the Sediment Transport Problem from General Physics. Geol. Surv. Prof. Paper vol. 422-I, US Geological Survey, DOI, USA.

Bijker, E., 1971. Longshore transport computations. ASCE Journal of Waterway, Port, Coastal and Ocean Engineering 97, 687–701.

Bos, K.J., Roelvink, J.A., Dingemans, M.W., 1996. Modelling the impact of detached breakwaters on the coast. Proceedings of the 25th International Conference on Coastal Engineering. ASCE, New York, pp. 2022–2035.

Dekker, S., Jacobs, C.E.J., 2000. Sediment Concentration Due To Irregular Waves and Currents. Master's thesis, Delft University of Technology, The Netherlands.

de Vriend, H.J., 1987. 2DH Mathematical modelling of morphological evolutions in shallow water. Coastal Engineering 11, 1–27.

de Vriend, H.J., Zyserman, J., Nicholson, J., Roelvink, J.A., Pechon, P., Southgate, H.N., 1993. Medium-term 2DH coastal area modelling. Coastal Engineering 21 (1–3), 193–224.

Dingemans, M.W., Radder, A.C., De Vriend, H.J., 1987. Computation of the driving forces of wave-induced currents. Coastal Engineering 11, 539–563.

Eckart, C., 1958. Properties of water: Part II. The equation of state of water and sea water at low temperatures and pressures. American Journal of Science 256, 225–240.

Forester, C.K., 1979. Higher order monotonic convective difference schemes. Journal of Computational Physics 23, 1–22.

Fredsoe, J., 1984. Turbulent boundary layer in wave–current interaction. ASCE Journal of Hydraulic Engineering 110, 1103–1120.

Gessler, D., Hall, B., Spasojevic, M., Holly, F., Pourtaheri, H., Raphelt, N., 1999. Application of 3D mobile bed, hydrodynamic model. Journal of Hydraulic Engineering, 737–749. July.

Grasmeijer, B.T., van Rijn, L.C., 1998. Breaker bar formation and migration. Proceedings of the 26th International Conference on Coastal Engineering, Copenhagen, Denmark. ASCE, New York, pp. 2750–2758.

Groeneweg, J., 1999. Wave–current interactions in a generalised Lagrangian Mean formulation. PhD thesis, Delft University of Technology, Delft, The Netherlands.

Groeneweg, J., Klopman, G., 1998. Changes of the mean velocity profiles in the combined wave–current motion in a GLM formulation. Journal of Fluid Mechanics 370, 271–296.

Hjelmfelt, A.T., Lenau, C.W., 1970. Nonequilibrium transport of suspended sediment. ASCE Journal of Hydraulic Division, 1567–1586. July.

Holthuijsen, L.H., Booij, N., Herbers, T.H.C., 1989. A prediction model for stationary, short-crested waves in shallow water with ambient currents. Coastal Engineering 13, 23–54.

Holthuijsen, L.H., Booij, N., Ris, R.C., 1993. A spectral wave model for the coastal zone. Proceedings of the 2nd International Symposium on Ocean Wave Measurement and Analysis, New Orleans, pp. 630–641.

Huang, W., Spaulding, M., 1996. Modelling horizontal diffusion with sigma coordinate system. Journal of Hydraulic Engineering 122 (6), 349–352.

Ikeda, S., 1982. Lateral bed-load transport on side slopes. ASCE Journal of the Hydraulic Division 108 (11), 1369–1373.

Isobe, M., Horikawa, K., 1982. Study on water particle velocities of shoaling and breaking waves. Coastal Engineering in Japan 25.

Kolmogorov, A.N., 1942. Equations of turbulent motion of an incompressible fluid. IZV Akad. Nauk. USSR, Ser. Phys., Vol. 6, pp. 56–58. (translated into English by D.B. Spalding, as Imperial College, Mechanical Engineering Department Report ON/6, 1968, London, U.K.).

Latteux, B., 1995. Techniques for long-term morphological simulation under tidal action. Marine Geology 126, 129–141.

Leendertse, J.J., 1987. A three-dimensional alternating direction implicit model with iterative fourth order dissipative nonlinear advection terms. WD-333-NETH, The Netherlands Rijkswaterstaat.

Lesser, G.R., 2000. Computation of Three-dimensional Suspended Sediment Transport within the DELFT3D-FLOW Module. MSc thesis No. HE066, IHE, Delft, The Netherlands.

Mellor, G.L., Blumberg, A.F., 1985. Modelling vertical and horizontal diffusivities and the sigma coordinate system. Monthly Weather Review 113, 1379–1383.

Nicholson, J., Broker, I., Roelvink, J.A., Price, D., Tanguy, J.M., Moreno, L., 1997. Intercomparison of coastal area morphodynamics models. Coastal Engineering 31, 97–123.

Partheniades, E., 1965. Erosion and deposition of cohesive soils. ASCE Journal of Hydraulic Division 91 (HY1), 105–139.

Péchon, P., Teisson, C., 1996. Numerical modelling of bed evolution behind a detached breakwater. Proceedings of the 25th International Conference on Coastal Engineering. ASCE, New York, pp. 2050–2057.

Prandtl, L., 1945. Uber ein neues formelsystem fur die ausgebildete turbulenz (On a new formation for fully developed turbulence). Nachrichten der Akademie der Wissenschaften (Report of Academy of Sciences, Gottingen, Germany), 6–19.

Rodi, W., 1984. Turbulence models and their application in hydraulics, State-of-the-art paper article sur l'etat de connaissance. Paper presented by the IAHR-Section on Fundamentals of Division II: Experimental and Mathematical Fluid Dynamics, The Netherlands.

Roelvink, D., Boutmy, A., Stam, J.M., 1998. A simple method to predict long-term morphological changes. Proceedings of the 26th International Conference on Coastal Engineering, Copenhagen. ASCE, New York, pp. 3224–3237.

Roelvink, J.A., Jeuken, M.C.J.L., van Holland, G., Aarninkhof, S.G.L., Stam, J.M.T., 2001. Long-term, process-based modelling of complex areas. Proceedings of the 4th Coastal Dynamics Conference, Lund, Sweden. ASCE, New York, pp. 383–392.

Ruessink, G., Miles, J., Feddersen, F., Guza, R.T., Elgar, S., 2001. Modeling the alongshore current on barred beaches. J. Geophys. Res. 106, 22451–22463.

Simonin, O., Uittenbogaard, R.E., Baron, F., Viollet, P.L., 1989. Possibilities and limitations to simulate turbulence fluxes of mass and momentum, measured in a steady stratified mixing layer. Proceedings XXIII IAHR Congress, Ottawa, August 21–25. National Research Council Canada, pp. A55–A62.

Soulsby, R.L., Hamm, L., Klopman, G., Myrhaug, D., Simons, R.R., Thomas, G.P., 1993. Wave–current interaction within and outside the bottom boundary layer. Coastal Engineering 21, 41–69.

Steijn, R., Roelvink, D., Rakhorst, D., Ribberink, J., van Overeem, J., 1998. North Coast of Texel: a comparison between reality and prediction. Proceedings of the 26th International Conference on Coastal Engineering, Copenhagen. ASCE, New York, pp. 2281–2293.

Stelling, G.S., 1984. On the construction of computational methods for shallow water flow problem. Rijkswaterstaat Communications vol. 35. Government Printing Office, The Hague, The Netherlands.

Stelling, G.S., Leendertse, J.J., 1991. Approximation of convective processes by cyclic AOI methods. Proceeding of the 2nd ASCE Conference on Estuarine and Coastal Modelling, Tampa. ASCE, New York, pp. 771–782.

Stelling, G.S., van Kester, J.A.T.M., 1994. On the approximation of horizontal gradients in sigma coordinates for bathymetry with steep bottom slopes. International Journal for Numerical Methods in Fluids 18, 915–955.

Stive, M.J.F., Wind, H.G., 1986. Cross-shore mean flow in the surf zone. Coastal Engineering 10, 235–340.

Struiksma, N., 1983. Results of movable bed experiments in the DHL curved flume. Report on Experimental Investigation. TOW Report R657-XVIII/M1771. Delft Hydraulics Laboratory, The Netherlands.

Struiksma, N., 1985. Prediction of 2-D bed topography in rivers. ASCE Journal of Hydraulic Engineering 111 (8), 1169–1182.

Struiksma, N., Olesen, K.W., Flokstra, C., de Vriend, H.J., 1984. Bed deformation in curved alluvial channels. Journal of Hydraulic Research 23 (1), 57–79.

Svendsen, I.A., 1985. On the formulation of the cross-shore wavecurrent problem. Proc. Workshop “European Coastal Zones”. National Technical University of Athens, Athens pp. 1.1–1.9.

Uittenbogaard, R.E., 1998. Model for Eddy Diffusivity and Viscosity Related to Sub-Grid Velocity and bed Topography. (unpublished note).

van Ledden, M., 2001. Modelling of SandMud Mixtures: Part II. A Process-Based SandMud Model. WL|Delft Hydraulics Report vol. Z2840. Delft Hydraulics, Delft, The Netherlands.

van Ledden, M., Wang, Z.B., 2001. Sand–mud morphodynamics in an estuary. River, Coastal and Estuarine Morphodynamics Conference, RCEM 2001 (IAHR), Japan. Springer, New York, pp. 505–514.

van Rijn, L.C., 1984. Sediment transport: Part II. Suspended load transport. Journal of Hydraulic Engineering 11, 1613–1641.

van Rijn, L.C., 1987. Mathematical Modeling of Morphological Processes in the Case of Suspended Sediment Transport. Delft Technical University, Delft, The Netherlands. (also Delft Hydraulics Communication No. 382).

van Rijn, L.C., 1993. Principles of Sediment Transport in Rivers, Estuaries and Coastal Seas. Aqua Publications, Amsterdam.

van Rijn, L.C., 2001 (October). Approximation Formulae for Sand Transport by Currents and Waves and Implementation in DELFT-MOR. WL|Delft Hydraulics Report vol. Z3054.20. Delft Hydraulics, The Netherlands (unpublished report for Rijkswaterstaat/RIKZ).

Verboom, G.K., Slob, A., 1984. Weakly reflective boundary conditions for two-dimensional water flow problems. 5th International Conference on Finite Elements in Water Resources, June 1984, Vermont, Adv. Water Resources vol. 7. Delft Hydraulics, Delft, The Netherlands. Delft Hydraulics Publication No. 322.

van Vossen, B., 2000. Horizontal Large Eddy Simulations; Evaluation of Computations with DELFT3D-FLOW. Report MEAH-197. Delft University of Technology, The Netherlands.

Walstra, D.J.R., Roelvink, J.A., Groeneweg, J., 2000. Calculation of wave-driven currents in a 3D mean flow model. Edge, B. Coastal Engineering vol. 2. ASCE, New York, pp. 1050–1063.

Watanabe, A., et al., 1986. Numerical prediction model of three-dimensional beach deformation around a structure. Coastal Engineering in Japan 29, 179–194.